the FEBS Journal

The alteration of the C-terminal region of human frataxin distorts its structural dynamics and function

Santiago E. Faraj[1], Ernesto A. Roman[1], Martin Aran[2], Mariana Gallo[2] and Javier Santos[1]

1 Instituto de Química y Físico-Química Biológicas, Universidad de Buenos Aires, Argentina
2 Fundación Instituto Leloir and IIBBA-CONICET, Buenos Aires, Argentina

Keywords
Friedreich's ataxia; molecular motions; NMR; protein folding; protein stability

Correspondence
M. Gallo, Fundación Instituto Leloir and IIBBA-CONICET, Av. Patricias Argentinas 435, 1405 Buenos Aires, Argentina
Fax: +054 11 5238-7501
Tel: +054 11 5238-7500
E-mail: marianagalletita@gmail.com
J. Santos, Instituto de Química y Físico-Química Biológicas, Universidad de Buenos Aires, Junín 956, 1113AAD, Buenos Aires, Argentina
Fax: +054 11 49625457
Tel: +054 11 49648290 (ext.108)
E-mail: javiersantosw@gmail.com

(Received 17 February 2014, revised 1 May 2014, accepted 6 June 2014)

doi:10.1111/febs.12869

Friedreich's ataxia (FRDA) is linked to a deficiency of frataxin (FXN), a mitochondrial protein involved in iron-sulfur cluster synthesis. FXN is a small protein with an α/β fold followed by the C-terminal region (CTR) with a nonperiodic structure that packs against the protein core. In the present study, we explored the impact of the alteration of the CTR on the stability and dynamics of FXN. We analyzed several pathological and rationally designed CTR mutants using complementary spectroscopic and biophysical approaches. The pathological mutation L198R yields a global destabilization of the structure correlating with a significant and highly localized alteration of dynamics, mainly involving residues that are in contact with L198 in wild-type FXN. Variant FXN 90–195, which is closely related to the FRDA-associated mutant FXN 81–193, conserves a globular shape with a native-like structure. However, the truncation of the CTR results in an extreme alteration of global stability and protein dynamics over a vast range of timescales and encompassing regions far from the CTR, as shown by proton–water exchange rates and ^{15}N-relaxation measurements. Increased sensitivity to proteolysis, observed *in vitro* for both mutants, suggests a faster degradation rate *in vivo*, whereas the enhanced tendency to aggregate exhibited by the truncated variant may account for the loss of functional FXN, with both phenomena providing an explanation as to why the alteration of the CTR causes FRDA. These results contribute to understanding how stability and activity are linked to protein motions and they might be useful for the design of target-specific ligands to control local protein motions for stability enhancement.

Introduction

Friedreich's ataxia (FRDA) is a hereditary disease that affects children and adolescents, characterized by progressive neurological impairment and cardiomyopathy. FRDA is highly associated with a deficiency in the expression or function of frataxin (FXN), an iron-binding protein critical for mitochondrial iron metabolism, global cellular iron homeostasis and antioxidant protection.

Human FXN is synthesized in the cytoplasm and imported into the mitochondria via a signal peptide. In this organelle, the protein is first processed to the intermediate FXN 42–210, and then to the mature

Abbreviations
CPMG, Carr–Purcell–Meiboom–Gill; CTR, C-terminal region; DTNB, 5,5′-dithiobis(2-nitrobenzoic acid); FXN, frataxin; hnNOE, heteronuclear ^{1}H-^{15}N NOE; HSQC, heteronuclear single quantum coherence; N, native state; PDB, Protein Data Bank; PFG, pulse field gradient; R_{ex}, contribution of the exchange to the transversal relaxation rate; R_h, hydrodynamic radius; SEC, size exclusion; T_1, ^{15}N spin-lattice relaxation time; T_2, ^{15}N spin-spin relaxation time; U, unfolded state.

form, FXN 81–210 [1,2]. Mature FXN plays an essential role in iron homeostasis; it may act as an iron chaperone delivering iron to enzyme partners during heme and Fe-S cluster biosynthesis [3–5].

The FXN structure comprises a globular domain that is present in all species and is preceded in eukaryotes by a flexible N-terminal tail of variable length and nonconserved sequence that contains the mitochondrial import signal. The average structure of the globular domain of human FXN (FXN 90–210) has already been resolved by NMR [6] and crystallography [7–9]. FXN 90–210 is composed of a five-stranded, antiparallel β-sheet and two parallel α helices forming an α/β sandwich, typical of the CyaY protein family [10]. Residues 196–210 constitute the C-terminal region (CTR), a segment that lacks periodic structure and packs against helices α1 and α2, occluding the apolar side chains of residues L198, L200, L203 and Y205. The CTR has been postulated as a key determinant of FXN fold stability [11]. In addition to van der Waals contacts, the CTR establishes a network of electrostatic interactions, including backbone–backbone and side chain–backbone hydrogen bonds, with itself and with the rest of the protein. Remarkably, the thermodynamic stability of FXN homologs is correlated with the length of the CTR [11]. A recent study suggested that, in addition, the CTR is crucial for determining FXN scaffold dynamics [12].

In most FRDA patients (~ 95%), an amplified GAA-repeat expansion is present within the first intron of both *fxn* alleles, resulting in the reduced transcription of the gene and ultimately leading to insufficient levels of FXN. In turn, the lack of FXN impairs incorporation of iron into the iron-sulfur cluster and heme cofactors, causing widespread enzymatic deficits and oxidative damage catalyzed by an excess of labile iron. In the remaining 5% of patients, the typical GAA expansion is present in only one *fxn* allele, whereas a missense mutation is found in the other allele. Although the disease course for these patients can be as severe as that for patients with two expanded alleles, the underlying pathophysiological mechanisms depend on mutation and are not completely understood. Few structural and functional details are known for missense mutations identified in FRDA patients. However, some of them have been studied, showing differences in their thermodynamic stability (e.g. stability of wild-type > W155R > I154F > D122Y > G130V), a propensity to aggregate (mutants I154F and W155R precipitate upon iron binding) and a lower Fe^{2+} binding stoichiometry (mutants D122Y and G130V) [13,14]. Interestingly, despite their decreased stabilities, NMR studies have shown that these clinical mutants retain a compact core and native-like dynamics [14]. In addition, for the N146K, Q148R and R165C FRDA missense mutations, it was shown that the FXN function is compromised in the binding and activating of the SDUF complex (consisting of proteins NFS1, ISD11, ISCU2 and FXN) for Fe-S cluster biosynthesis [7].

Although FXN is markedly resistant to proteolysis, a short peptide involving the last six residues of the CTR is removed by chymotrypsin [12], suggesting that this part of the CTR is quite mobile, in contrast to the rigidity of the rest of the FXN domain that remains unaltered. This is in agreement with results obtained from structure-based simulations [12].

Interestingly, L198R, a point mutation located in the CTR that introduces a positive charge in the apolar interaction surface between the CTR and residues from both helices, has been found in FRDA patients [15]. Moreover, a frame shift mutation yielding the truncated form FXN 81–193 determines FRDA with a rapid disease progression [16]. Accordingly, and based on our experience with the truncated variant FXN 90–195, which lacks the CTR [12], we hypothesized that the interaction of the CTR with the globular domain of FXN is critical for its stability and function. Furthermore, we proposed that the absence of the CTR or, as in the case of the L198R mutant, a weakened interaction with the compact globular domain, should have an impact on the dynamics of the protein, finally leading to destabilized and nonfunctional molecules.

In a broader context, the complex relationships that govern the interplay between protein stability and dynamics are a matter of continuous study and debate. To meaningfully address this issue, it is important to acknowledge the differences between global and local events that may govern various phenomena in a protein. In this framework, FXN constitutes an excellent model for studying the links between protein motions and thermodynamic stability.

Furthermore, an interesting dilemma of general interest is whether a significant alteration in global stability of FXN originates the complete alteration of protein motions. On the other hand, a change in stability may produce a specific effect on localized regions of the protein, causing only a local adjustment of molecular dynamics. This is particularly relevant given the possibility of designing target-specific ligands to control local protein motions for stability enhancement [17].

From this perspective, we hypothesized that global protein stability and dynamics are linked phenomena. The present study aimed to test this assumption, using the human frataxin as a model. Specifically, we analyzed the correlation between protein stability and

motions in wild-type FXN (FXN 90–210) and in FXN variants carrying mutations in the CTR with the aim of understanding the role of the CTR in the stability and dynamics (and ultimately in the function) of FXN. We prepared the truncated variant FXN 90–195 and the pathological variant FXN L198R. In addition, we rationally designed and produced mutants FXN L198A and L198C (to explore in detail the contribution of side-chain contacts established by this residue) and L200C and L203C (to investigate local dynamics by thiol accessibility in different positions of the CTR). Protein motions over diverse timescales were investigated by NMR spectroscopy, proteolysis and molecular dynamics simulations. The global stability of each FXN variant was studied by thermal and chemical equilibrium unfolding experiments. Local solvent exposition was investigated by solvent proton exchange kinetics measurements applying NMR techniques. Our results indicate that the mutation L198R and the complete truncation of the CTR in FXN produce an increase of local and global dynamics, respectively, leading to thermodynamically destabilized proteins. These factors contribute to loss of function of FXN in FRDA patients, suggesting that these alterations could be targeted pharmacologically to improve protein folding and stability.

Results

Design of the CTR mutants

To investigate the consequences on protein dynamics and stability of different mutations in the CTR of FXN, we prepared several variants (Fig. 1). First, we produced the pathological L198R mutant that introduces a positively-charged amino acid in the place of an apolar residue. In addition, we prepared variant L198A as a model of the truncation of the L198 side chain to explore the magnitude of the contribution to protein stability of the apolar interactions established by L198, as well as variant L198C, which not only introduces a shorter side chain than Leu, but also locates a thiol in this position, in an effort to further investigate the molecular motions at this site by thiol-exchange. Furthermore, to explore local variations in the dynamics and in the interactions of the CRT, we also studied the Cys mutants L200C and L203C. Finally, the effects of these mutants were compared with the effect of completely removing the CTR in the more drastic variant FXN 90–195, which is closely related to the FRDA-associated mutant FXN 81–193. Variant FXN 90–210, nine residues shorter in its N-terminal region than the mature form FXN 81–210, was the wild-type control sample for FXN conformation, stability and dynamics.

All mutants are monomeric and globular in solution and display a native-like fold; only FXN 90–195 shows a tendency to aggregate at high protein concentrations

Wild-type FXN and all the mutants were successfully expressed and purified. FXN 90–210 and FXN 90–195, as well as variants FXN L198R, L198A, L198C, L200C and L203C, all behave as monomeric and globular proteins as indicated by size exclusion (SEC)-FPLC, dynamic light scattering and diffusion NMR experiments (Table 1). The measured effective hydrodynamic radius (R_h) for the wild-type protein, obtained by pulse field gradient (PFG)-NMR experiments using dioxane as an internal standard [18] of 18.7 ± 0.2 Å agrees, within the experimental error, with SEC-FPLC and dynamic light scattering measurements (18.9 ± 0.5 Å), as well as with the expected R_h calculated from the

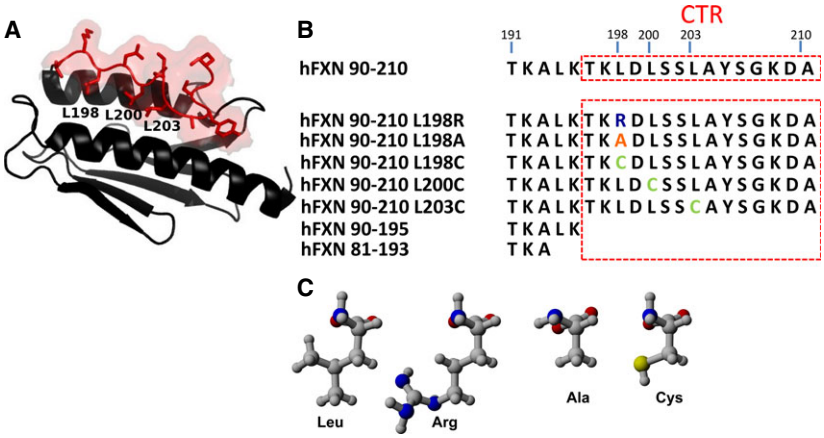

Fig. 1. Human frataxin variants. (A) Ribbon model of FXN. Residues L198, L200 and L203 are indicated as sticks and CTR is shown in red (B) Sequence detail of FXN variants investigated in the present study. The C-terminal sequence of Friedreich's ataxia variant FXN 81–193, which lacks the last 17 amino acid residues, is also shown. A representation (sticks and balls) of the different side-chains evaluated at position 198 in the present study is shown in (C).

Table 1. Hydrodynamic radii of FXN variants.

Method	Protein concentration (μM)	FXN 90–210 (nm)	FXN 90–210 L198R (nm)	FXN 90–195 (nm)
Dynamic light scattering	80	1.89 ± 0.05	1.94 ± 0.19	1.82 ± 0.03[c]
PFG-NMR	300–600	1.87 ± 0.02	1.93 ± 0.04	2.30 ± 0.05
Prediction using the MW[a]		1.86	1.86	1.78
Prediction using the crystallographic structure[b]		1.87		

[a] Assuming a globular shape, the R_S of the native state of a given protein is calculated using the equation: log (R_S) = −(0.254 ± 0.002) + (0.369 ± 0.001) × log (MW), where MW is the molecular weight expressed in Da and the hydrodynamic radius is in Å according to Uversky [58].

[b] HYDROPRO [19,26] and PDB code: 1EKG were used.

[c] Value taken from Roman *et al.* [12].

crystallographic structure [19]. We have previously shown the compact and monomeric hydrodynamic behavior of FXN 90–195, with a radius somewhat smaller than that obtained for FXN 90–210 (18.2 ± 0.3 Å, protein concentration of 80 μM), in concordance with the expected value for a globular protein of that size [12]. It is noteworthy that a small proportion of unfolded molecules may be present in solution as a result of the marginal stability of this variant, distorting the estimation of the R_h of the native-state [12]. However, when the R_h was measured by PFG-NMR at 300 μM, the value obtained was meaningfully larger (23.0 ± 0.5 Å); the dependence of the R_h on protein concentration is an indication of the propensity to auto-associate in solution. By contrast, for the single point mutant FXN L198R, the R_h obtained (19.3 ± 0.4 Å) was slightly larger than that of the wild-type protein, and it was not dependent on the protein concentration.

Fluorescence and CD spectra show that the overall conformation of variant FXN L198R and of all point mutants investigated in the present study is approximately native-like (Fig. 2). The maximal wavelength (λ_{max}) of Trp fluorescence is ~ 337 nm, indicating that

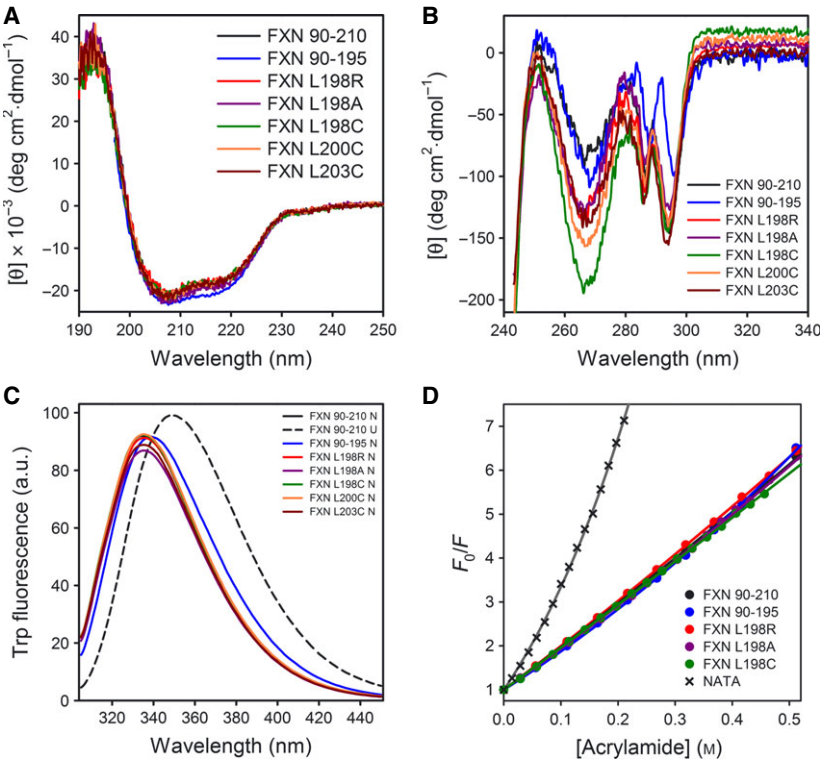

Fig. 2. Spectroscopic characterization of the FXN variants. (A) Far-UV CD, (B) near-UV CD and (C) tryptophan fluorescence emission spectra. The measurements were carried out at 20 °C in buffer 20 mM Tris-HCl, 100 mM NaCl, 1 mM EDTA (pH 7.0). (D) Accessibility of Trp residues in FXN 90–210, FXN L198R and FXN 90–195. Stern–Volmer plots for the quenching of Trp fluorescence by acrylamide. Trp fluorescence was measured by excitation at 295 nm and emission was collected between 305 nm and 450 nm. FXN 90–210 (black), FXN 90–195 (blue), L198R (red), L198A (violet), L198C (green), L200C (orange) and L203C (brown). Unfolded FXN 90–210 is included (dashed lines in C).

the emission occurs from an apolar environment, whereas, at a urea concentration of 8.0 M, λ_{max} shifts to 352 nm, which is compatible with the complete unfolding of the protein. In addition, far- and near-UV CD spectra show that the secondary structure content and tertiary packing are similar to wild-type FXN. However, the absence of the CTR in FXN 90–195 might produce more pronounced and long-range effects, as indicated by the change in the λ_{max} of Trp fluorescence (~ 339 nm) and the attenuation of CD bands in the near-UV region in comparison with the wild-type FXN.

The global packing of frataxin variants was explored by evaluating Trp accessibility via fluorescence quenching experiments with acrylamide. As shown in Fig. 2D, there are no differences in quenching among FXN 90–210, FXN 90–195 and FXN L198R, indicating that, in these variants, Trp residues are, on average, packed in a similar way. This is consistent with compact proteins in solution.

To analyze the conformation (and dynamics, see below) of FXN variants at the amino acid residue level by NMR, we prepared ^{15}N labeled FXN 90–210, FXN L198R and FXN 90–195. The ^{1}H-^{15}N heteronuclear single quantum coherence (HSQC) spectra of the three FXN samples display a good chemical shift dispersion (Fig. 3A), which is a sign of well-folded proteins.

FXN 90–210 exhibits a spectrum of excellent quality, which is very similar to the one reported previously [6]. Similarly, FXN L198R displays a good HSQC spectrum, with the expected number of peaks, all of them well dispersed and with uniform line widths. By contrast, FXN 90–195 shows inhomogeneous line

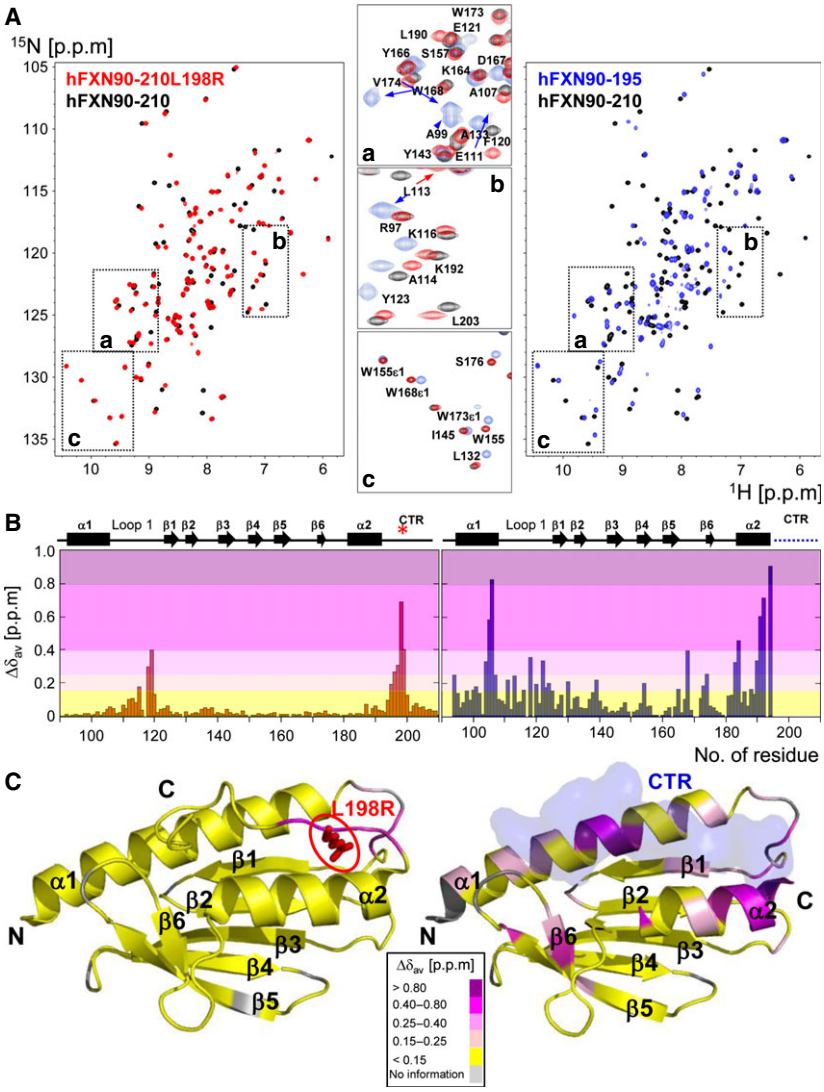

Fig. 3. Chemical shift assignment of FXN variants. (A) Superposition of the ^{1}H-^{15}N HSQC spectra of FXN L198R (left, red) and FXN 90–195 (right, blue) with wild-type FXN 90–210 (black). In the central panel, the insets show selected regions of the spectra in which the chemical shift assignment is indicated. (B) The average chemical shift differences ($\Delta\delta_{av} = [(\Delta\delta^2_{NH} + \Delta\delta^2_N/25)/2]^{1/2}$) between FXN 90–210 and FXN L198R (left) and between FXN 90–210 and FXN 90–195 (right) are plotted against the residue sequence. Regions of secondary structure in FXN are shown in the upper part. (C) Values from B are mapped on the FXN 90–210 crystal structure (PDB code: 1EKG) with a color gradient encoding the magnitude of the shift changes. Position 198 and the CTR region are indicated.

width and some overlapping of peaks, especially in the central region of the HSQC. Furthermore, the number of observed peaks for the truncated version is larger than expected, indicating conformational heterogeneity of the sample. The observed inhomogeneous line width and the presence of additional signals in the spectrum are symptomatic of the existence of alternative conformations in equilibrium in solution, which are in intermediate/slow exchange on the NMR timescale. Nevertheless, a major well-folded population of FXN 90–195 was identified in the NMR spectra and assigned. We also detected approximately thirty extra signals less intense and with poor chemical shift dispersion, suggesting that they correspond to one or more not well-folded population(s) of the protein (Fig. 4). Thus, the presence of the CTR stabilizes FXN folding, whereas, when absent, the protein appears to explore a vaster conformational space.

We assigned the α and amide proton and nitrogen resonances of variant FXN L198R and of the main conformation of FXN 90–195 using the available chemical shifts of the full-length C-terminal domain of FXN (BMRB 4342) as a starting point, as well as ^{15}N-edited NOESY and TOSCY spectra. In uncertain cases, the ^{15}N-NOESY spectrum of FXN 90–210 was also helpful for confirming the assignment between close crosspeaks. For FXN L198R, the first two N-terminal residues and S129 and G170 were not observed because they are solvent exposed, and thus not detected in our experimental conditions. For the assignment of the most populated conformation of FXN 90–195, the NOESY spectrum, and especially the sequential $NH_{i-1}NH_i$ crosspeaks in the helical regions, was essential. In this case, the first four residues and T119, S129, G170 and K171 were also not detected as a result of exchange with the solvent. A105 was probably broadened beyond detection as a result of slow conformational motions because the nearby residues show relatively large crosspeaks. The average chemical shift differences between the amide signals of wild-type FXN and mutants are plotted as a function of the amino acid sequence in Fig. 3B and the results are mapped on the crystallographic structure of the globular domain of FXN in Fig. 3C. For mutant FXN L198R, the differences with respect to the wild-type protein were, as expected, less significant when compared with the truncated protein FXN 90–195, and mainly restricted to the residues near R198 in the CTR and in loop 1 (connector of α1 and β1 elements). Moreover, the most perturbed residues in FXN L198R displayed a reduced intensity in the HSQC spectrum, probably as a result of conformational instability in this stretch or a higher solvent exposition as a consequence of the mutation. The largest deviations were observed for the truncated protein, with major differences located in both helices, which contact the CTR in the wild-type FXN structure. However, loop 1, strands β1, β5 and β6, and loop β5β6 also exhibit significant chemical shift differences in the shorter variant with respect to FXN 90–210, even though these stretches do not directly interact with the CTR in the wild-type protein. This result suggests that the presence of the CTR has a long-range influence over the conformation and stability of the protein. Nevertheless, a comparative NOESY pattern analysis of FXN 90–195 and FXN 90–210 indicates that the secondary structure of the protein is mainly preserved in the former (i.e. medium NH_{i-1}-NH_i, $H\alpha_{i-3}$-NH_i NOE interactions for α-helices and strong $H\alpha_{i-1}$-NH_i NOE interactions for β-strands). Especially, sequential NH_{i-}

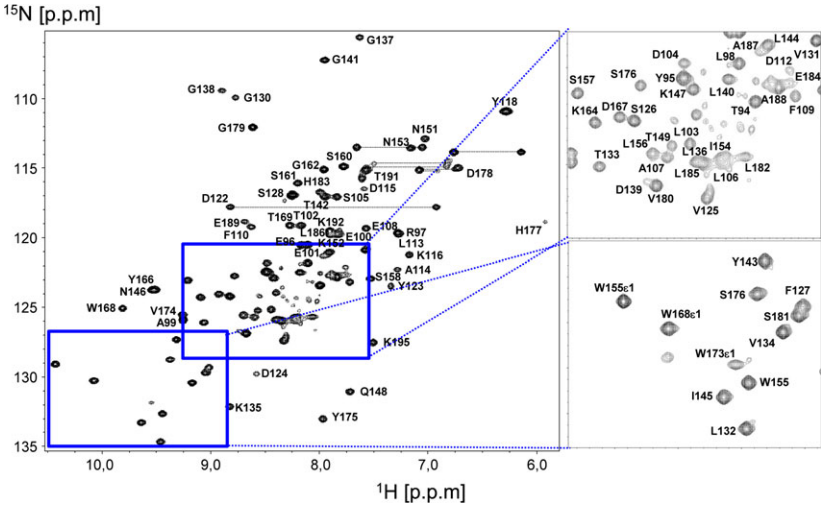

Fig. 4. Detail of the ^{1}H-^{15}N HSQC spectrum of FXN 90–195. The chemical shift assignment of the major conformation is indicated. The insets show selected regions of the spectrum in which additional crosspeaks were detected. The extra signals are less intense and dispersed compared to those of the assigned main conformation, indicating that they correspond to one or more alternative less populated and probably not well folded conformation(s) also present in solution.

$_1$-NH_i crosspeaks in the α-helical regions were of great help in the chemical shift assignment. Furthermore, TALOS+ [20] analysis of chemical shift values shows that the secondary structure of FXN is preserved in the FXN 90–195 and FXN L198R variants (data not shown).

CTR mutants display reversible unfolding but reduced stability with respect to the wild-type protein

To investigate whether point mutation L198R destabilizes the native conformation of FXN 90–210, chemical and temperature equilibrium unfolding experiments were performed (Fig. 5 and Tables 2–4). Both types of experiments confirmed that FXN L198R is highly destabilized. C_m and T_m parameters significantly dropped to lower denaturant concentration and lower temperature values, respectively. Remarkably, as in the case of wild-type FXN, unfolding was reversible [12], as indicated by signal recovery after cooling the samples. Urea-induced unfolding of FXN L198R is compatible with a reduction in the free energy of unfolding of ~ 4.2 kcal·mol^{-1} (Tables 2 and 3). Although the CTR is not necessary for the consolidation of FXN fold [12], these results reveal the key function of the CTR in conferring FXN with global stability, and indicate the role of the apolar side chain of residue L198 with respect to contributing to stabilizing interactions between the CTR and the rest of the domain.

To further explore the role of L198 side-chain contacts, we also replaced this residue by Ala and Cys. These mutations significantly destabilized the proteins, as seen in urea unfolding experiments ($\Delta\Delta G_{NU}$ values are 2.5 and 1.0 kcal·mol^{-1}, respectively) and temperature-induced unfolding experiments. Moreover, the truncated variant is greatly destabilized by comparison with the wild-type FXN and even its stability [12] is lower than that of L198R (Tables 2 and 3). Thus, the stabilities of FXN variants are: FXN 90–195 < L198R < L198A < L198C < wild-type (Fig. 5C and Table 4). This result is compatible with the fact that the Cys side chain can establish interactions via its -SH group [21,22], whereas variant L198A carries a shorter side chain, deleting a number of native contacts.

Moreover, as previously described for equilibrium unfolding of wild-type FXN [12,13], all full-length variants studied in the present study exhibit unfolding curves compatible with a two-state model (N U), as indicated by the shape and the overlapping of CD and Trp fluorescence curves. A global fitting of the two-state model, taking into account a unique m_{NU} parameter (the dependence of free energy on denaturant concentration) for all full-length variants, was

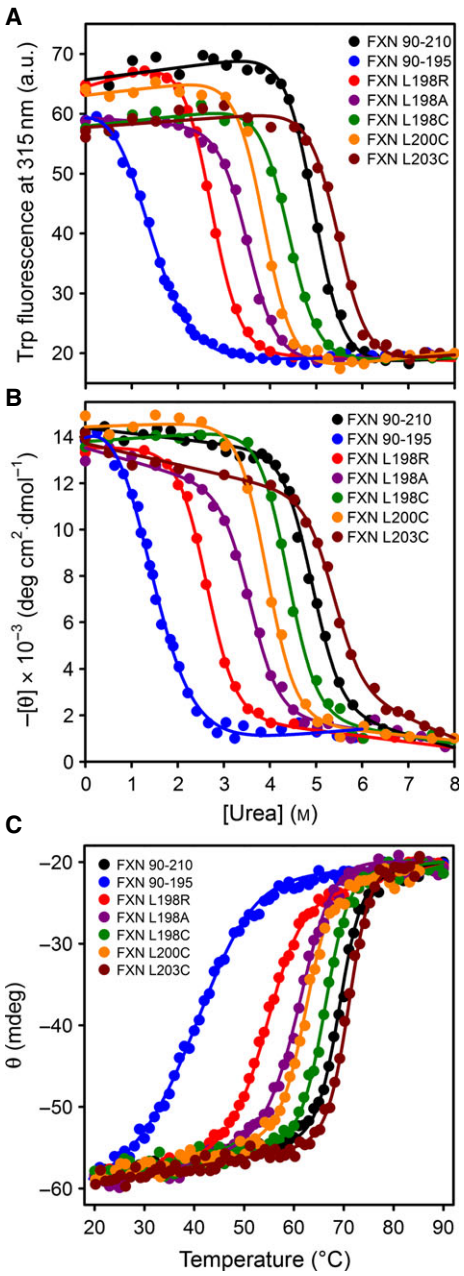

Fig. 5. Equilibrium unfolding experiments followed by (A) tryptophan fluorescence and (B) far-UV CD of FXN variants. Proteins were incubated in urea (in buffer 20 mM Tris-HCl, 100 mM NaCl, 1 mM EDTA, pH 7) for 3 h, and measurements were carried out at 25 °C. (C) Thermal unfolding followed by CD at 220 nm; experiments were carried out in 20 mM sodium phosphate, 100 mM NaCl (pH 7.0). Solid lines represent the nonlinear regression fitting of the two-state model to the data. FXN 90–210 (black), L198R (red), L198C (green), L198A (violet), L200C (orange), L203C (brown) and FXN 90–195 (blue).

Table 2. Two-state model fitting (N↔U). Urea unfolding of FXN variants followed by Trp fluorescence. A global fitting simultaneously including fluorescence and CD experiments was performed for full-length variants allowing a unique m_{NU} value. The obtained value for m_{NU} is considerably larger than the value inferred from the sequence of the protein (1.83 ± 0.05 and 1.45 kcal·mol^{-1}·M^{-1}, respectively). For FXN 90–195 m_{NU} = 1.26 ± 0.13.

FXN variant	$\Delta\Delta G°_{NU(H20)}$ (kcal·mol^{-1})[a]	$\Delta G°_{NU(H20)}$ (kcal·mol^{-1})	C_{mNU} (M)
90–210 (wild-type)	–	9.2 ± 0.2	4.9 ± 0.04
L198R	4.2 ± 0.3	5.0 ± 0.1	2.70 ± 0.04
L198A	2.6 ± 0.3	6.5 ± 0.2	3.52 ± 0.04
L198C	1.0 ± 0.3	8.1 ± 0.2	4.40 ± 0.04
L200C	2.0 ± 0.3	7.2 ± 0.2	3.88 ± 0.04
L203C	−1.0 ± 0.3	10.1 ± 0.3	5.48 ± 0.04
90–195	7.6 ± 0.3	1.5 ± 0.2	1.2 ± 0.15

[a] $\Delta\Delta G°_{NU(H20)} = \Delta G°_{NU(H20)\ wild\text{-}type} - \Delta G°_{NU(H20)\ mutant\ i}$.

Table 3. Two-state model fitting (N↔U). Chemical unfolding of FXN variants followed by far-UV CD at 220 nm. Fitting was performed as described in Table 2.

FXN variant	$\Delta\Delta G°_{NU(H20)}$ (kcal·mol^{-1})[a]	$\Delta G°_{NU(H20)}$ (kcal·mol^{-1})	C_{mNU} (M)
Wild-type	–	9.1 ± 0.2	4.90 ± 0.04
L198R	4.2 ± 0.3	4.8 ± 0.2	2.62 ± 0.04
L198A	2.5 ± 0.3	6.6 ± 0.2	3.57 ± 0.04
L198C	1.0 ± 0.3	8.1 ± 0.2	4.37 ± 0.04
L200C	1.8 ± 0.3	7.3 ± 0.2	3.92 ± 0.04
L203C	−0.9 ± 0.4	9.9 ± 0.3	5.37 ± 0.04
90–195	7.5 ± 0.3	1.6 ± 0.2	1.27 ± 0.14

[a] $\Delta\Delta G°_{NU(H20)} = \Delta G°_{NU(H20)\ wild\text{-}type} - \Delta G°_{NU(H20)\ mutant\ i}$.

performed. The obtained m_{NU} was considerably larger than the value inferred from the size of FXN (Tables 2 and 3). This explains the discrepancy between free-energy values reported in the present study for wild-type FXN and previous work by our laboratory [12], where the predicted m_{NU} value for this protein [23] was used to calculate $\Delta G°_{NU\ H2O}$.

In addition, the dependence of stability on pH (in the range 6–8) was investigated. Although we found no pH effect on the stability of the wild-type and FXN 90–195 variants [12], the introduction of a thiol group in the case of Cys mutants might alter protein stability at a pH near the pK_a because the thiol is being stabilized as a thiolate (-SH →-S$^-$). The introduction of a negative charge might therefore disturb the apolar environment of the Cys. The results show that, in this range of pHs, there is no change in the stability of the FXN variants (data not shown), suggesting that, even at pH 8.0, the thiolate group is not significantly populated in this environment.

Table 4. Two-state model fitting (N↔U). Temperature unfolding of FXN variants followed by far-UV CD at 220 nm. A global fitting was performed for full-length variants, allowing for a unique value of the difference in heat capacity between native and unfolded states (ΔC_{PNU} = 1.81 ± 0.3 kcal·mol^{-1}·K^{-1}). For variant FXN 90–195, which was fitted independently, ΔC_{PNU} was 1.02 ± 0.5 kcal·mol^{-1}·K^{-1}.

FXN	ΔH_{NU} (kcal·mol^{-1})	T_m (°C)	ΔG_{NU} at 25 °C (kcal·mol^{-1})
Wild-type	104.2 ± 9.6	69.4 ± 0.4	8.04 ± 1.2
L198R	56.8 ± 7.4	54.1 ± 0.8	2.6 ± 0.7
L198A	63.8 ± 8.5	61.1 ± 0.8	3.2 ± 0.9
L198C	100.7 ± 8.5	66.1 ± 0.3	7.5 ± 1.0
L200C	86.5 ± 7.7	62.3 ± 0.3	5.7 ± 0.8
L203C	108.9 ± 9.9	71.0 ± 0.4	8.7 ± 1.3
90–195	26.6 ± 8.1	39.9 ± 3.6	0.9 ± 0.4

The thiol reactivity of single-cysteine CTR mutants suggests a relationship between stability and dynamics

To explore the effect of the alteration of the interaction network established by residues located in the CTR on the local dynamics, we studied the reactivity of the thiol group placed in positions 198, 200 and 203 (Fig. 6). Although variants L198C, L200C and L203C are stable proteins, they show a gradual change in global stabilities compared to the wild-type protein ($\Delta\Delta G°_{NU\ H2O}$ = 1.0, 2.0 and −1.0 kcal·mol^{-1}, respectively) (Tables 2 and 3). Interestingly, the mutants display significant differences in reactivity towards 5,5′-dithiobis(2-nitrobenzoic acid) (DTNB). When a thiol is located at position 198, it exhibits a significantly lower reactivity than the thiol in position 200. On the other hand, when the thiol is located at position 203, the global stability of the protein increases in comparison with the wild-type, whereas the reactivity of the C203 residue is the lowest of the three mutants. This effect on the stability of mutation L203C is not predicted by the FOLDX algorithm [24], suggesting that a conformational change at the level of the backbone might take place in the case of this mutation. In addition, the reactivity of the three mutants is drastically lower than the one observed for a free -SH group of β-mercaptoethanol (Fig. 6).

Therefore, the thiol reactivity of the single-cysteine CTR mutants suggests that the specific perturbation of the hydrophobic interactions between the CTR and

the core of the FXN leads to changes in global stability and dynamics of the CTR.

CTR mutants exhibit an increment of internal motions on several timescales

To study the effect of the L198R mutation on FXN flexibility, we performed a limited proteolysis experiment with chymotrypsin followed by RP-HPLC-MS (Fig. 7).

Although FXN 90–210 shows a marked resistance to proteolysis, after 4 h of incubation, we detected a single cutting site at the Y205 position. By contrast, the L198R mutation enhances sensitivity to the protease. Even at a very short incubation time (30 s), almost 50% of the protein is cut at the Y205 position (Fig. 7). After 2 min, proteolysis at this unique site increases, and longer incubations lead to multiple cuts along the polypeptide chain. Increased sensitivity to proteolysis resembles values previously observed for FXN 90–195 [12]. Thus, increased susceptibility to proteolysis of mutant L198R indicates that some disorder or local breathing is induced when the CTR is not present or when it is not stably packed against the globular domain. By contrast, variants L198A, L198C, L200C and L203C, similar to the wild-type protein, present substantial resistance to proteolysis (data not shown).

To explore the characteristics of the pathological mutation L198R and to study the effect of the CTR truncation on the overall backbone dynamics of FXN

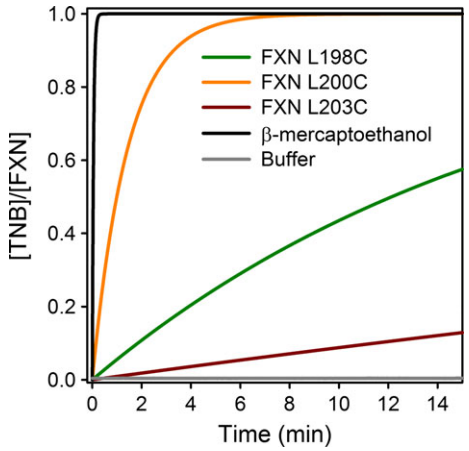

Fig. 6. The reactivity of the free thiol of variants L198C (green) and L200C (orange), L203C (brown), reaction mixture in buffer alone (gray) and of the free-thiol model β-mercaptoetanol (black) is shown. Protein (or β-mercaptoethanol) and DTNB concentrations were 30 and 500 μM, respectively. Measurements were performed at 25 °C in buffer 20 mM Tris-HCl, 100 mM NaCl (pH 7.0).

at a residue level, we performed ^{15}N relaxation measurements on ^{15}N-FXN L198R, ^{15}N-FXN 90–195 and ^{15}N-FXN 90–210 (Fig. 8). As reported previously [14], the C-terminal domain of wild-type FXN exhibits rather uniform values of the relaxation rates along the protein sequence, a sign of a compact globular protein. Indeed, the <hnNOE> value is 0.81 ± 0.07, with only the C-terminus experiencing significantly lower values than average (Fig. 8B). The N-terminus is not observed in the spectra as a result of high solvent exposition. Therefore, except for this stretch, FXN 90–210 does not undergo fast internal motions on the nanosecond/picosecond timescale under our experimental conditions. Furthermore, the experimental T_1/T_2 ratios are very similar to those predicted by the crystallographic structure using HYDRONMR software [25,26] (Fig. 8A). HYDRONMR considers global diffusion, including anisotropic tumbling effects as a result of the structure, although it ignores internal dynamics, assuming a completely rigid structure. The calculated T_1/T_2 ratios agreeably reproduce the experimental T_1/T_2 profile at the residue level with an RMSD value of 0.65 between the calculated and experimental values of these ratios. The only residues of the protein displaying relative high T_1/T_2 ratios and a shorter T_2 are those in the V134–G141 region, comprising the β2–β3 loop, and T149 belonging to the loop β3–β4, suggesting the presence of low-frequency motions, as often are associated with conformational exchanges. Finally, the correlation time (τ_C), as estimated from the T_1/T_2 ratio [27], is 8.3 ns, which is in relative good agreement with the value calculated from the crystallographic structure (8.0 ns) [25,26] and the previously reported value (7.9 ns) [14]; differences may be a result of dissimilarities in the experimental conditions. Thus, FXN is a rigid and compact molecule mainly lacking accentuated internal motions.

For variant L198R, the T_1/T_2 ratios present almost the same average value of the wild-type protein, considering only residues of the rigid core. This is translated into a τ_C value for the L198R mutant of 8.2 ns, which is very similar to the value obtained for wild-type FXN under the same experimental conditions, and consistent with comparable hydrodynamic properties for both molecules. Furthermore, the general T_1/T_2 trend along the polypeptide sequence is similar to that of the wild-type protein, indicating that the tertiary structure of the protein is also mainly conserved in the mutant. However, in this case, there are some regions that display differences in the relaxation values with respect to the wild-type protein (Fig. 8A,B). Most of the residues with the largest deviations in the T_1/T_2 ratio with respect to the mean value are located near

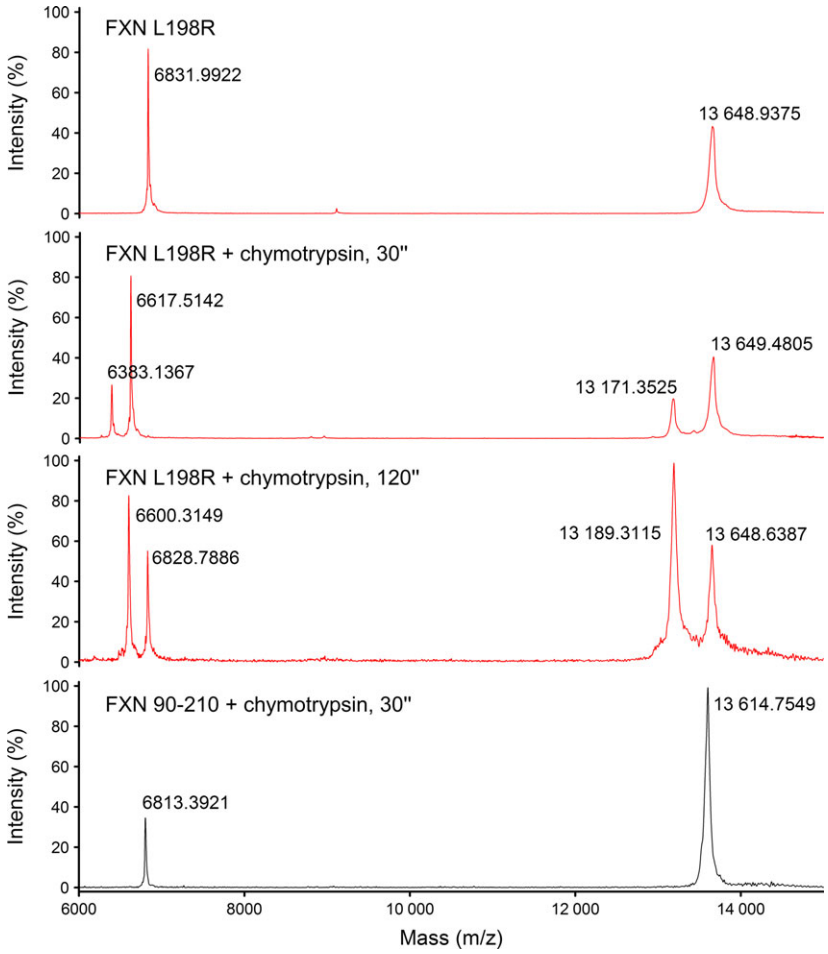

Fig. 7. Controlled proteolysis of FXN 90–210 and mutant L198R followed by MS. Protein Samples of 1.0 mg·mL^{-1} (chymotrypsin 1 : 200, protease : protein mass ratio) were incubated for 0 s, 30 s or 2 min at 20 °C in buffer 20 mM Tris-HCl, 100 mM NaCl, 0.1 mM EDTA (pH 7.0). The reactions were stopped and samples were submitted to MALDI-MS.

position 198 in the protein structure and show positive variations as a result of reduced T_2 relaxation times. This suggests the presence of low-frequency (microsecond/millisecond) motions in these regions as a consequence of the L198R mutation. These results are consistent with the hnNOE profile for the mutant, which is less scattered than the T_1/T_2 data. Indeed, hnNOE is sensitive to fast but not to slow internal motions. The <hnNOE> value for this variant is 0.81 ± 0.08, which is very similar to that of the wild-type protein. Residues S105 and A188 in helices α1 and α2, respectively, are the exception, exhibiting a significant reduction of the T_1/T_2 ratio, as well as hnNOE values indicative of more flexibility on the fast timescale.

A comparison of the dynamics of mutant L198R with that of the wild-type protein is summarized and mapped on the Protein Data Bank (PDB) structure of FXN (Fig. 8C). In general, the mutant has a more dynamic behavior than the wild-type protein. The former not only displays predominantly slow conformational dynamics, but also presents some residues with fast internal motions in regions that are close to the introduced positive charge, such as the CTR itself and regions that are in contact with it (helix α2, strand β6 and loop 1).

The effect of mutations L198R, L198C and L198A on FXN dynamics was also investigated by all-atom molecular dynamics simulations. Runs showed that there are no large conformational alterations (Fig. 9A). However, for mutants L198R and L198A, a highly dynamic (nanosecond regimen) region involving loop1 is predominantly identified, as indicated by the higher RMSF values at the level of backbone Cα atoms of residues 113–124 (Fig. 9C). As expected, the more drastic mutant L198R shows high RMSF values in residues near the mutation (Figs 9B,C).

As a result, replacing a Leu for an Arg in position 198 not only affects the stability of the domain, but also the internal dynamics of the polypeptide, which nevertheless exhibits similar secondary and tertiary structures to those of the wild-type protein. An

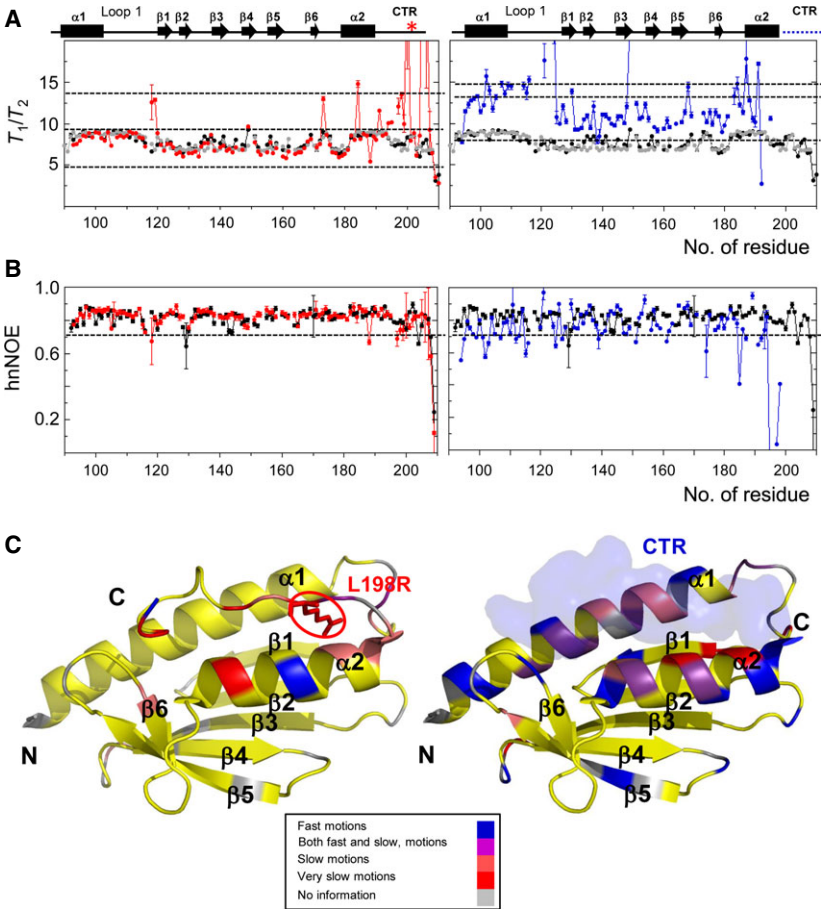

Fig. 8. Backbone dynamics of FXN variants. ^{15}N-^{1}H relaxation was measured on FXN L198R (red), FXN 90–195 (blue) and FXN 90–210 (black). The ^{15}N T_1/T_2 ratio as a function of the protein sequence for each variant is shown in (A), whereas ^{15}N-^{1}H NOE values are shown in (B). In addition, T_1/T_2 values were predicted from the crystallographic structure using HYDRONMR [25] (gray color). (C) Motions are mapped on the PDB 1EKG structure for FXN L198R (left) and FXN 90–195 (right). Residues experiencing fast motions (picosecond/nanosecond), with ^{15}N-^{1}H NOE values smaller than 0.7, are shown in blue. Residues with slow conformational motions (microsecond/millisecond) are depicted as: amino acids exhibiting T_1/T_2 values higher than the mean value plus 1 SD, in red; amino acids with T_1/T_2 values larger than 1 SD plus the mean value taken from residues that have T_1/T_2 values in the $<T_1/T_2>$ + SD range, in light red. Residues that exhibit both fast and slow internal motions, with increased T_1/T_2 and reduced hnNOE values, are shown in violet. Finally, residues for which we do not have dynamical information are shown in gray.

increase in the flexibility of the polypeptide chain occurs on several timescales and is observed in regions that are located near the CTR, which is chiefly affected.

Regarding FXN 90–195, we observed signs of degradation in the NMR spectra after keeping the protein solution for 3 days at 22 °C, suggesting a certain degree of instability. Therefore, we aimed to study the internal motions in this variant, analyzing the ^{15}N relaxation measurements performed at a protein concentration of 0.3 mM, despite the propensity of this mutant to auto-associate at high protein concentrations (see above). Under these conditions, the signal to noise relationship is good and no degradation was detected after spectra acquisition. Figure 8A,B reports the T_1/T_2 ratio and the hnNOE values along the protein sequence. A visual inspection of the relaxation data shows that the values are more scattered than in the wild-type protein and that the mean T_1/T_2 ratio for FXN 90–195 is significantly higher than the values observed for the wild-type and L198R proteins (11.0 for the truncated protein versis ~ 8 for wild-type and L198R FXN, under the same experimental conditions). We attribute this difference in the mean values mainly to the tendency exhibited by the truncated protein to aggregate, thus generating a larger apparent rotational correlation time, given that it exists in solution as a bigger object in average at high concentrations. However, a contribution to the T_1/T_2 ratio obtained for the truncated protein of possibly local unfolding events in fast exchange with the folded conformation cannot be excluded either.

Nevertheless, the internal motions are still analyzable from the relaxation data. Indeed, not only T_1/T_2, but also hnNOE values are very scattered, with a <hnNOE> of 0.76 ± 0.13. Fast motions are observed in loops (loop 1, β2β3, β3β4, β4β5 and β5β6) and in both helices, as well as at the termini of the protein. On the other hand, reduced T_2 values suggest slow conformational motions involving loop 1 and loop β3β4, strands β1 and β5, and helices α1 and α2. These regions appear to be more flexible than the mobile regions in FXN L198R, without considering the CTR, which is not present in the truncated protein. Remarkably, some of these regions (Fig. 8C) are not in contact with the CTR in the wild-type protein, suggesting

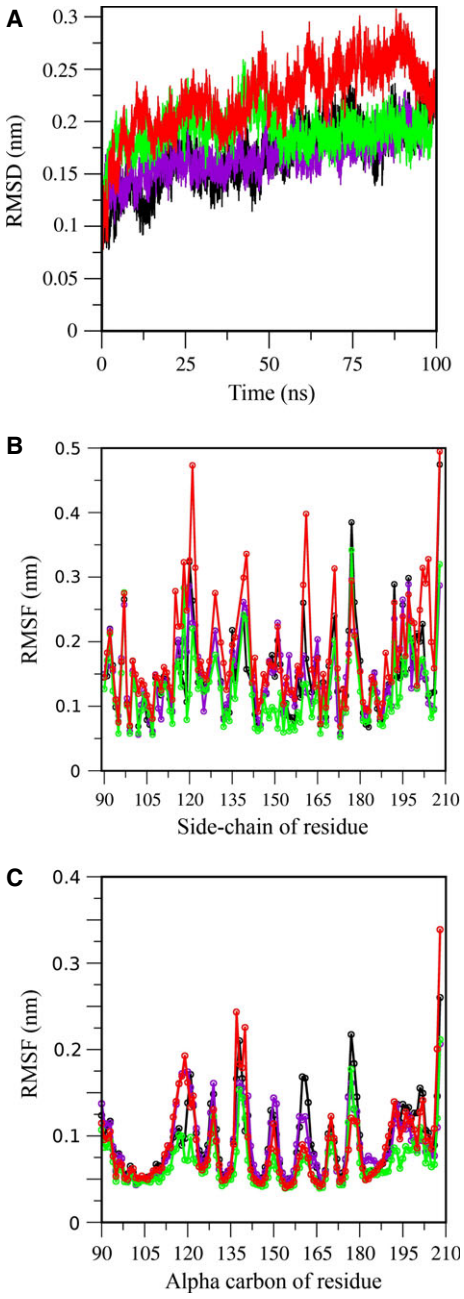

Fig. 9. All atom molecular dynamics simulations of FXN 90–210 (black) and L198R (red). L198A (violet) and L198C (green). (A) RMSD and RMSF values per amino acid residue for the side chain (B) and Cα atoms (C) were computed from the equilibrated part of the trajectory.

the existence of long-range dynamic effects produced by the removal of the CTR.

Therefore, the CTR-truncated protein exhibits a tendency to aggregate at high protein concentrations, and backbone dynamics reveal significant flexibility on both the picosecond/nanosecond and microsecond/millisecond timescales in residues that map near the CTR, as well as in more distant regions.

Relaxation dispersion experiments also demonstrate a distinct behavior for FXN variants, indicating a different contribution of the conformational exchange to the transversal relaxation rates

To complete the dynamic characterization of FXN variants, ^{15}N Carr–Purcell–Meiboom–Gill (CPMG) relaxation dispersion experiments were performed. These experiments are useful for monitoring conformational exchange processes in the slow time window (0.3–10 ms) and for detecting weakly populated protein states that are often not directly observable in NMR spectra. CPMG relaxation dispersion senses processes occurring in the intermediate–fast regime ($k_{ex} \approx \Delta\nu$), resulting in enhanced relaxation rates ($R_2^{Obs} = R_2^0 + R_{ex}$), provided that there is substantial chemical shift difference among the exchanging states [28]. The dependence of ^{15}N transverse relaxation rates on the strength of an applied radio frequency spin-lock (ν_{CPMG}) was evaluated for FXN 90–210, FXN L198R and FXN 90–195. Typical dispersion curves are shown in Fig. 10A. The exchange broadening can be estimated from the height of the dispersion curve [i.e. from the difference between R_2^{Obs} at the lowest ν_{CPMG} ($\nu_{CPMG} \rightarrow 0$) and the value registered at the highest ν_{CPMG} ($\nu_{CPMG} \rightarrow \infty$)]. The measured values are displayed along the protein sequence in Fig. 10B for the three FXN variants. The median of ΔR_2^{Obs} values increases from 0.60 and 0.72 s^{-1} in FXN 90–210 and FXN L198R, respectively, to 2.88 s^{-1} for the truncated variant. Residues with a significant R_{ex} contribution to the transversal relaxation rate are mapped on the crystallographic structure in Fig. 10C.

The wild-type protein exhibits exchange motions in the region comprising helix α1, loops β2β3 and β3β4 (which also show relatively short T_2 values) and strands β3, β4 and β6.

FXN L198R experiences exchange in the same regions than the wild-type protein, as well as in R198 and nearby residues. Particularly, amino acids in the helix α2 and in the CTR exhibit considerable R_{ex} contributions, as also suggested by T_2 measurements. On the other hand, FXN 90–195 shows higher ΔR_2 values than the other variants. Regions that are subjected to exchange contribution in the wild-type protein also exhibit substantially higher R_{ex} values. In addition, stretches with altered residues are distributed all over the protein structure, the C-terminus of helix α1, helix α2, loops α1β1, β1β2 and β2β3, and strand β5, are

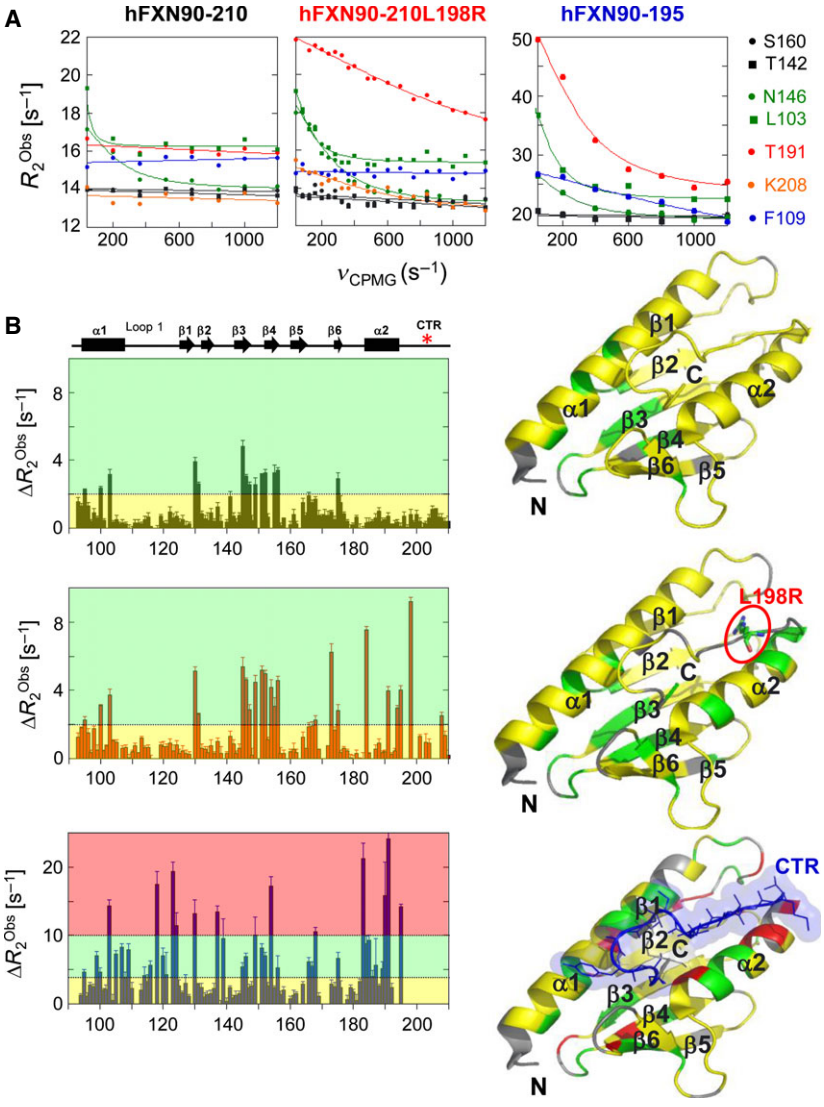

Fig. 10. Chemical exchange contributions measured by CPMG NMR. (A) Representative CPMG relaxation dispersion profiles for FXN 90–210, 90–195 and L198R. Lines correspond to the optimal global fit of the Meiboom equation to the experimental data. Residues S160 and T142 (black) do not show chemical exchange in any variant. By contrast, N146 and L103 (green) exhibit chemical exchange contributions in all variants. T191 (red) exchanges in the mutants but not in the wild-type protein. K208 (orange) belongs to the CTR and exchanges only in L198R. Finally, F109 (blue) shows an exchange in FXN 90–195 but not in the other variants. (B) The exchange contribution to transverse relaxation, ΔR_2^{Obs}, estimated from the difference in R_2^{Obs} at the lowest and highest ν_{CPMG} values, is plotted along the protein sequence for FXN 90–210 (top), FXN L198R (medium) and FXN 90–195 (bottom). An exchange threshold of 2 s^{-1} is indicated by a dotted line for FXN 90–210 and L198R. For FXN 90–195, exchange thresholds of 4 and 10 s^{-1} are indicated. (C) Results are mapped on the FXN 90–210 crystal structure for the three proteins.

also involved in exchange motions. Thus, on this timescale, both mutants exhibit a more dynamic behavior in localized regions near the mutation in FXN L198R and all over the protein structure, with substantially increased R_{ex} values in FXN 90–195. This result is consistent with the ^{15}N R_1 and R_2 measurements indicating that the truncated protein is able to explore a vaster conformational ensemble than the wild-type and the single point mutant FXN counterparts.

FXN 90–195 presents higher global solvent accessibility than FXN 90–210, whereas FXN L198R differs only in regions spatially near the mutation

We estimated the relative solvent exchange rates for backbone amide groups by measuring the ζ_{NOE} effect with the solvent using the water-NOE experiment [29,30]: the higher the ζ_{NOE} values, the larger the solvent exchange rates (see Materials and methods). The results for FXN 90–210 are shown in Fig. 11. Regions exposed to the solvent are the N-terminal stretch of helix α1 (indeed, the two N-terminal residues of the protein are not observable in NMR experiments), loops β1β2, β4β5, β5β6 and β6α2. Also, residues K197, D199, S201 and G207 from the CTR exhibit relatively high solvent exchange rates compatible with an increase in solvent accessibility. This behavior matches very well with the accessibilities inferred from FXN structure (data not shown).

Figure 12 shows the differences between ζ_{NOE} values obtained for FXN L198R and FXN 90–195 and those obtained for the wild-type protein ($\Delta\zeta_{NOE} = \zeta_{NOEmut} - \zeta_{NOEwt}$). Amino acids exhibiting

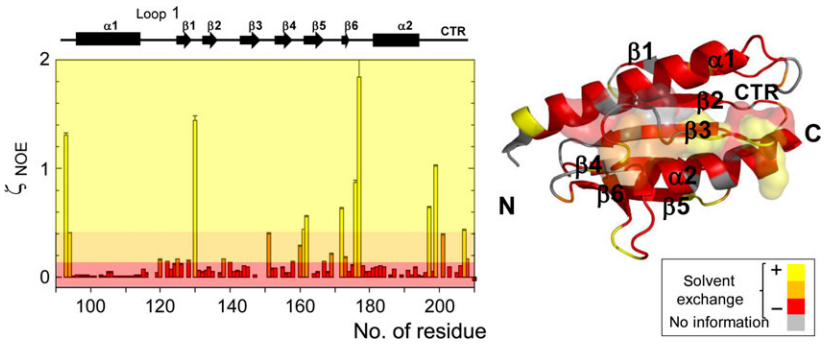

Fig. 11. Amide proton-water exchange rates of FXN 90–210 (wild-type). ζ_{NOE} values as a function of the residue number. Residues showing larger $\Delta\zeta_{NOE}$ values are less protected from solvent exchange. Results are mapped on the FXN 90–210 crystal structure (right).

positive $\Delta\zeta_{NOE}$ values are more protected from solvent exchange in the wild-type protein, whereas the reverse is true for those showing a negative $\Delta\zeta_{NOE}$. For the L198R mutant, regions with increased solvent accessibility are localized in loops α1β1 (loop1) and β5β6, and, in the CTR, all of them spatially near position 198 in the wild-type protein. By contrast, most residues exhibit positive $\Delta\zeta_{NOE}$ values in FXN 90–195, indicating that the amide protons of this variant are globally less protected from solvent exchange than those of the wild-type protein. The greatest differences in water exchange are observed for the helix α1, the C-terminal stretch of helix α2, and loops α1β1 (loop 1), β4β5 and β6α2, which contact the CTR in FXN 90–210. However, positive $\Delta\zeta_{NOE}$ also appear in the β-sheet residues. These results show an overall increase of the solvent exposure in the truncated variant and are in agreement with the mutant being highly destabilized, exhibiting a more dynamic behavior, and probably possessing local breathing that allows an increased exchange with the solvent. By contrast, in the case of FXN L198R, differences in the solvent exchange rates are localized and limited to regions that are close to the mutation.

Iron binding is completely altered in FXN variants

Wild-type FXN 90–210 is able to maintain iron in a soluble and bioavailable state. We investigated whether FXN 198R and the truncated variant are equally able to bind iron. Each variant was incubated with $FeCl_3$ and, subsequently, the soluble iron was quantified (Fig. 13A). At pH 7.0, and in the absence of protein, Fe^{3+} quantitatively precipitates in the first few minutes after mixing (Fig. 13A). Remarkably, neither FXN 90–195, nor FXN L198 were able to maintain the same iron concentrations in the soluble state to the

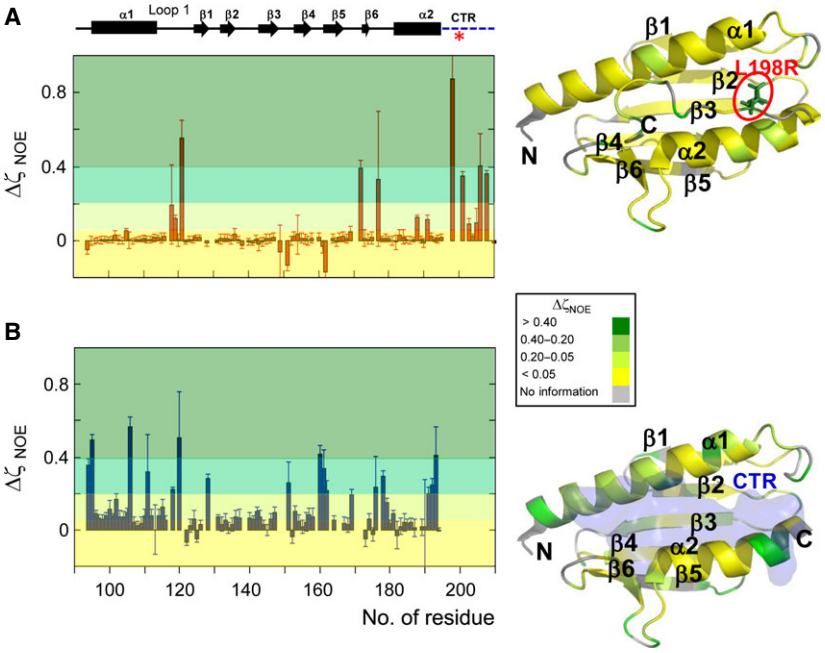

Fig. 12. Amide proton-water exchange rates of the mutants. (A) Difference between ζ_{NOE} values of FXN L198R and FXN 90–210, $\Delta\zeta_{NOE} = \zeta_{NOE}$ (FXN L198R) − ζ_{NOE} (FXN 90–210). (B) Difference between ζ_{NOE} values of FXN 90–195 and FXN 90–210, $\Delta\zeta_{NOE} = \zeta_{NOE}$ (FXN 90–195) − ζ_{NOE} (FXN 90–210). Residues showing a positive $\Delta\zeta_{NOE}$ are more protected from solvent exchange in wild-type FXN, whereas the reverse is true for those showing a negative $\Delta\zeta_{NOE}$. Results are mapped on the FXN 90–210 crystal structure (right).

same extent as wild-type FXN. To establish whether this was a result of protein aggregation during the incubation, the protein concentration was checked by SDS/PAGE (Fig. 13A, inset). No significant protein precipitation was observed after a 2-h incubation (more than 80% of the protein remains soluble). Taking into account the iron-binding capability of BSA, this protein was analyzed in the same way. In addition, hen egg-white lysozyme was included in the experiment as a negative control.

Furthermore, to estimate the stoichiometry in which hFXN variants maintain Fe^{+3} solubity and bioavailability, we incubated increasing protein concentrations of each hFXN variant with a high and fixed concentration of the metal ion (250 μM). Estimations taking into account the minimal protein concentration that maintains the maximal iron concentration (Fig. 13B) indicate that wild-type protein is able to bind at least four Fe^{3+} atoms per protein molecule under these experimental conditions, whereas FXN 90–195 and FXN L198R maintain one iron atom at most. These results should be considered an approximation given that free Fe^{3+} precipitates and, consequently, the system is out of equilibrium. The decreased thermodynamic stability and the enhancement of internal dynamics in the variants, added to the iron-binding deficiency, help to explain why the biological function of the point mutant L198R and the FRDA-associated variant FXN 81–193 (mimicked in the present study by FXN 90–195) should be drastically altered.

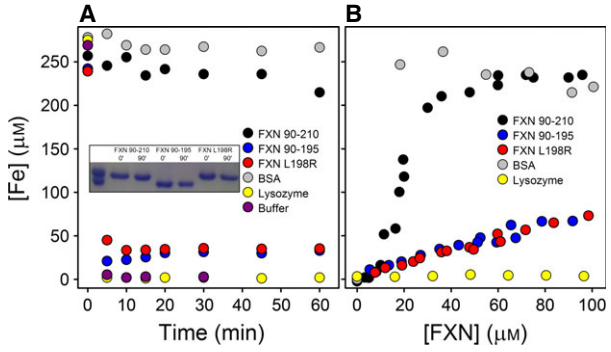

Fig. 13. Iron-binding capability of FXN variants. (A) Each variant (50 μM) was incubated with 250 μM $FeCl_3$, and soluble iron was quantified along the incubation time. Inset: Protein aggregation was checked after 0 or 90 min of incubation by SDS/PAGE. (B) Proteins at increasing concentrations were incubated for 30 min with 250 μM $FeCl_3$. All experiments were performed in buffer: 50 mM Hepes, 50 mM NaCl, pH 7.0 at 25 °C. Wild-type (black), FXN 90–195 (blue) and FXN L198R (red). In addition, BSA (gray), lysozyme (yellow) and buffer without protein (violet) were included as control samples.

Discussion

Motions and thermodynamic stability are important features of protein function and there may be connections among them [31,32]. However, biologically relevant protein motions may span a very large timescale, ranging from picoseconds to milliseconds, seconds and minutes. This fact often makes any understanding of this relationship rather challenging. From a structural point of view, protein motions are involved in very different processes: rotamer selection, backbone rearrangements, local unfolding and even global unfolding/refolding transitions. In this context, changes in the dynamics of the native state can affect protein–protein and protein–substrate interactions and *in vivo* stability that, in the case of FXN, is particularly relevant in FRDA [13,33].

Protein motions on the fast timescale (picosecond/nanosecond) are linked to thermodynamics by their contribution to conformational entropy. In particular, by the reduction of the difference in entropy between unfolded and folded ensembles, proteins can increase their thermodynamic stability [34]. Slow motions (microsecond/millisecond timescale) are related to function (conformational changes) and allostery (intramolecular signal transduction). In functional proteins, rigidity and flexibility should be balanced within a certain conformational stability. The observation of proteins with high stability, as well as enhanced flexibility and conformational heterogeneity [35], indicates that the relationships between molecular motions and stability may be more complex than a simple inverse relation where the increase in molecular fluctuations determines a decrease in stability. In the same fashion, the thermostable protein rubredoxin from *Pyrococcusfuriosus* (characterized by a T_m of ~ 200 °C and very slow unfolding kinetics) shows indistinguishable conformational flexibility from that of typical mesophilic proteins, as indicated by hydrogen exchange experiments that capture conformational fluctuations within the timescale of hydrogen bond rupture (the conformational opening for solvent access occurs in the millisecond time frame or faster at 28 °C for all amide positions) [36].

These results open the possibility that conformational fluctuations and protein motions may be only weakly coupled to global dynamics (folding/unfolding). By contrast, as shown by Whitley *et al.* [37], these properties may be coupled. They demonstrated that mutations of the CI2 protein cause backbone and side chain dynamics alterations. When the mutation is located in the folding-nucleus core of the protein, it may affect the dynamics (picosecond/nanosecond) of the N-terminal half, thus influencing flexibility

throughout the whole protein. Remarkably, CI2 mutants show an enhancement of the side-chains motions (picosecond/nanosecond) by comparison with the wild-type CI2. This increase in motions is globally distributed, suggesting a manifestation of cooperativity in dynamics.

Protein dynamics of human FXN in the picosecond/nanosecond range were previously studied by NMR [14,38]. Longitudinal and transverse relaxation rates and hnNOE indicated that FXN behaves as a rather rigid and compact globular protein with internal motions on the picosecond/nanosecond timescale at both termini. Thus, as in the case of CI2 among many other proteins, wild-type human FXN appears to have evolved to a high level of rigidity that may assist in function. Results obtained from proteolysis experiments are in line with this notion [12–14].

In the present study, it was shown that the experimental T_1/T_2 ratios neatly reproduce the predicted values calculated from the crystallographic structure. However, despite the fact that wild-type human FXN is mainly a rigid protein, our results show some slow conformational motions in the approximately millisecond timescale survey. They comprise a region involving helix α1 (included in the acidic ridge compromised in iron binding), strands β3 and β4, the loop in-between, and loop β1β2. These last regions are not directly involved in iron binding (the iron-binding site is an acidic surface containing the C-terminus of helix α1, strand β1 and loop 1) but might be involved in other protein functions or interactions.

Regarding the CTR, in the wild-type protein residues K197, D199, S201 and G207 exhibit relatively high solvent exchange rates. The relatively high exposition of these residues is in agreement with the cutting site at Y205 observed only after long incubation times with chymotrypsin. In a previous study [12], we showed that the CTR confers FXN with stability and also that this stretch might modulate protein dynamics, including FXN folding rates. Remarkably, the finding that a frame shift produces the truncation of FXN at residue 193 (Fig. 1) and determines FRDA with rapid disease progression [16] indicates that the CTR is crucial for the biological function of FXN. Furthermore, the CTR point mutation L198R has been found in FRDA patients [15], suggesting a key role for this stretch. The L198 side chain interacts with residues from helix α1 (F109 and L113), helix α2 (L190 and L194), loop 1 (Y118) and the CTR (L200, T196 and T191), establishing a large network of tertiary contacts. The introduction of a positive charge in this hydrophobic environment may weaken the interaction of the CTR with the compact globular domain.

In the present study, we studied stability/motions relationships in wild-type protein and FXN variants carrying mutations in the CTR to further explore the link between these properties and to gain insight on the role of the CTR in the stability and function of FXN. Therefore, in addition to the pathogenic variant L198R and the truncated FXN 90–195, we prepared variants L198A, L198C, L200C and L203C. All mutations, with the exception of L203C, lead to some degree of destabilization. By contrast to the other mutants, L203C is 1.0 kcal·mol^{-1} more stable than the wild-type protein and the thiol group in this position presents the lowest reactivity toward DTNB. A Cys in this position (C203) may optimize contacts with the side chain of S105 and the carbonyl group of L200, slightly strengthening the interaction between the core and the CTR. In connection with this result, higher pK_a values than expected for exposed -SH groups are predicted using the H++ algorithm [39] (> 12 for the three variants) and PROPKA [40,41] (10.2, 11.5 and 9.7 for C198, C200 and C203, respectively) for *in silico* prepared variants. Taken together, these results are in agreement with the notion that the cluster of apolar interactions established between the CTR and the α1/α2 secondary structure elements is a potential modulator of FXN motions, and suggest that local/specific changes on the dynamics of the CTR may be controlled by a local perturbation of stability.

The L198R mutation yielded a global destabilization of protein structure and a significant alteration of the dynamics of the CTR and helix α2 (on the microsecond/millisecond timescale) and loop1 (on the picosecond/nanosecond timescale). In addition, the exchange rates with the solvent of the CTR and loop1 also increased upon mutation. Furthermore, a slightly larger R_h than the wild-type protein is consistent with some disorder or local breathing in this stretch of the protein. The residues that change their motions upon L198R mutation are in contact with L198 in wild-type FXN, thus indicating that the adjustments in protein motion caused by this change in the protein structure are highly localized. Furthermore, changes in local stabilities (measured by hydrogen exchange) appear to co-localize with an increment of the internal motions in residues located near the mutation. As loop1 forms part of the acidic ridge (α1, loop1 and β1), changes in dynamics of this region may cause the observed defective function for this variant. Furthermore, significant reduction in thermodynamic stability and enhanced sensitivity to proteolysis observed *in vitro* for mutant L198R might be a cause of *in vivo* degradation.

Although the stability/dynamics/function link fits with our results, simpler direct interaction between

wild-type CTR and the SDUF complex might also explain the functional deficiency of the CTR mutants. However, the available structural information indicates that FXN could interact with the rest of the SDUF complex through regions different from the CTR. The interaction involves direct recognition of the negatively-charged region of FXN by the positively-charged patch of the cysteine desulfurase [42–44]. This makes it less likely that any direct interaction between CTR and the complex would mediate SDUF activation, even though we cannot fully rule out this possibility. In human FXN, the last stretch of CTR might act with helix-α1 as a structural building block.

Although variant FXN 90–195 conserves a globular shape with native-like secondary structure, the complete truncation of the CTR not only results in a significant alteration in global stability, but also derives in an extensive alteration of protein dynamics analyzed by proton-water exchange rates and ^{15}N relaxation measurements. The enhanced motions include regions far from the CTR and occur over a vast range of timescales. This is in contrast to other pathological variants, such as D122Y, G130V, I154F and W155R, for which relaxation measurements have shown that, although T_1/T_2 ratios vary as a result of aggregation, hnNOE values remain similar [14]. This behavior of the truncated protein may indicate that, under these experimental conditions, it explores a substantially larger conformational space than wild-type FXN and L198R mutant. This space might include high-energy intermediate states and unfolded conformations. This is also evident from the ^{15}N ^{1}H HSQC spectrum of FXN 90–195 showing that other minor conformations of the protein, which might be partially folded, coexist in solution, in equilibrium with the main well-folded one. Taking into account that the difference in free energy between the folded and unfolded states (20 °C) for the truncated form is ~ 1.0–1.3 kcal·mol^{-1}, the unfolded fraction in equilibrium might be ~ 5–15%.

In line with the destabilization induced by the absence of the CTR, a sticky character of this variant was shown at high protein concentrations. More likely, truncation of the CTR leaves some hydrophobic side chains exposed to the solvent, and molecules tend to interact minimizing the accessible apolar surface when the concentration of the protein rises. It is noteworthy that the truncated form exhibits a large destabilization of the FXN fold, making it more probable to cross the unfolding activation barrier. More importantly, regarding the functionality of FXN, for both FXN L198R and FXN 90–195, the most distorted regions include helix α1 and loop1, which contain a number of putative iron-binding sites. This behavior is also congruent with the higher sensitivity to proteases previously observed for the truncated variant, which includes one proteolytic site in loop1 [12]. Remarkably, both the truncated variant and the point mutant L198R exhibit a drastically altered iron-binding capability, by comparison with wild-type FXN.

Taken together, these results contribute to explain why the alteration of the CTR in L198R mutant [15], or its complete truncation in FXN 81–193 [16], causes FRDA. The greater destabilization observed for the truncated protein is in agreement with the atypical clinical phenotype of FXN 81–193, which exhibits a strikingly rapid disease progression [16]. In this context, we propose that a better understanding of the complex inter-relationships between protein flexibility and stability should enable the rational design and optimization of protein formulation conditions based on protein dynamics. Finally, we suggest that these alterations might be targeted pharmacologically to improve protein folding and stability.

Materials and methods

Protein expression, purification and refolding

Unlabeled FXN 90–210, FXN 90–195, FXN L198R, L198A, L198C, L200C and L203C were expressed and purified as described previously [12]. ^{15}N-labeled proteins (~ 50 mg·L^{-1} of cell culture with a protein purity ≥ 95%) were prepared in *Escherichia coli* cultures grown in M9 minimal medium, supplemented with ^{15}N-NH_4Cl obtained from Cambridge Isotope Laboratories (Andover, MA, USA). The ESI ion trap mass spectrometer (Thermo Finnigan, San José, CA, USA) was used to confirm the expected masses of unlabeled and labeled proteins. Purity was checked by SDS/PAGE.

Limited proteolysis

FXN variants (1 mg·mL^{-1}) were incubated with chymotrypsin at a mass ratio of 1 : 100, (protein : protease), at 25 °C in a buffer containing 20 mM Tris-HCl, 100 mM, NaCl, 1 mM EDTA (pH 7.0). Aliquots were separated at different times and the reaction was immediately stopped by an addition of 0.2% trifluoroacetic acid and 1.0 mM phenylmethanesulfonyl fluoride. Samples were kept at −20 °C until analysis by SDS/PAGE and RP-HPLC followed by MALDI-TOF or ESI-MS.

Fluorescence measurements

Steady-state fluorescence measurements were performed in a Jasco FP-6500 spectrofluorometer (Jasco Inc., Easton, MD, USA) operating in the ratio mode and equipped

with a thermostated cell holder connected to a circulating water bath set at 25 °C. A cell with a path length of 0.3 cm and sealed with a Teflon cap was used. Intrinsic fluorescence of proteins was measured using a protein concentration of 10 μM; excitation wavelength was 295 nm and emission data were collected in the range 305–450 nm. The spectral slit-widths were set to 3 nm for both monochromators.

Quenching experiments were carried out using acrylamide. Results were analyzed according to a modified version of the Stern–Volmer equation [45]:

$$\frac{F_0}{F} = (1 + K_{sv} \times [Q]) \times e^{([Q] \times v)} \quad (1)$$

where F_0 and F are the fluorescence intensity in the absence and presence of quencher, respectively, $[Q]$ is the concentration of the quencher, and V is the volume of the sphere of action (the volume immediately surrounding the excited fluorophore within which instantaneous quenching occurs). Quenching within this volume is called static quenching and can also arise from equilibrium association between the quencher and the fluorophore. The Stern–Volmer constant, K_{SV}, describes the dynamic quenching process and is the result of the mean fluorescence lifetime in the absence of quencher times the bimolecular collisional rate constant. The K_{SV} and V values were obtained by fitting Eqn (1) to experimental data using a nonlinear least-squares procedure.

CD measurements

CD measurements were carried out with a Jasco J-810 spectropolarimeter calibrated with (+) 10-camphor sulfonic acid. Near-UV and far-UV CD spectra were collected using cells with path lengths of of 1.0 and 0.1 cm, respectively. Data were acquired at a scan speed of 20 nm·min^{-1} and at least three scans were averaged. Finally, blank (buffer) scans were subtracted from the spectra and values of ellipticity were converted to molar ellipticity. The protein was used at a concentration of 10 μM, in buffer of 20 mM Tris-HCl, 100 mM NaCl (pH 7.0).

Thiol accessibility

Chemical reactivity toward DTNB was determined at 25 °C in a buffer of 20 mM Tris-HCl, 100 mM NaCl (pH 7.0).

A DTNB solution of 2.0 mg·mL^{-1} (5 mM) was prepared in a 100 mM sodium phosphate buffer, 1 mM EDTA (pH 7.0). Protein was used at a concentration of 30 μM and 50 μL of DTNB stock was added to begin the reaction in a final volume of 500 μL. Absorbance was monitored in thermostated cells at 412 nm. β-mercaptoethanol was used to precisely quantify the DTNB concentration and as a free-thiol model to establish the experimental conditions. A blank without protein was run to subtract the absorbance of the reaction mixture (without any thiol group) at 412 nm.

Protein unfolding experiments

Isothermal unfolding experiments were carried out incubating FXN with 0–8.0 M urea in a buffer solution of 20 mM Tris, 100 mM NaCl (pH 7.0) for 3 h at room temperature. All measurements were carried out at 25 °C. The process was followed by far-UV CD and tryptophan fluorescence measurements. To calculate thermodynamic parameters, a two-state unfolding mechanism, where only native (N) and unfolded (U) conformations exist at equilibrium, was assumed. Data processing was performed in accordance with the methods of Santoro and Bolen [46]. In addition, unfolding transitions as a function of temperature were monitored by the CD signal at 220 nm. Experiments were carried out in 20 mM sodium phosphate, 100 mM NaCl at a pH 6.0, 7.0 and 8.0. Protein concentration was 7.0 μM and a cell with a path length of 1.0 cm was used. Temperature was varied from 10 to 90 °C, at a constant rate of 1 °C·min^{-1}, sampling at intervals of 1 °C. To extract the thermodynamic parameters, the following model was fitted to the data:

$$\Delta G_{NU} = -RT\ln\left(\frac{f_U}{f_N}\right) = \Delta H_{T_m} + \Delta C_P(T - T_m) - T\left(\left(\frac{\Delta H_{T_m}}{T_m}\right) + \Delta C_P \ln\left(\frac{T}{T_m}\right)\right) \quad (2)$$

$$S = f_N(S_{0,N} + l_N T) + f_U(S_{0,U} + l_U T) \quad (3)$$

where f_U and f_N are the unfolded and folded fractions at equilibrium, respectively; T_m is the temperature at which $f_U = f_N$; S is the observed CD signal; $S_{0,N}$ and $S_{0,U}$ are the intrinsic CD signals for the native and unfolded states, respectively; and l_N and l_U are the slopes of the pre- and post-transition regions, respectively, assuming a linear dependence of S_N and S_U with temperature [47].

Explicit-solvent all atom molecular dynamics simulations

To investigate the fast conformational dynamics of FXN 90–210 and FXN L198R (in the range of picoseconds to nanoseconds), simulations with GROMACS 4.5.4 and GROMOS 53a6 force fields were carried out [48,49]. For the wild-type FXN, the initial structure was generated from the coordinates of the crystallographic structure PDB code: 1EKG. In the case of the L198 mutants, protein was mutated and minimized using FoldX 'buildmodel' engine and 'repair' protocol to energetically minimize the new structure [24]. The structure of each protein was embedded in a dodecahedral periodic cell with a minimum distance of 0.9 nm

between the protein atoms and the cell limits. Both structures were solvated with simple point charge water molecules. Sodium and chloride ions were added up to a 150 mM salt concentration. One thousand steps of energy minimization were performed. Then, 10 000 steps of position restrained simulations were carried out to equilibrate water molecules. A canonical ensemble simulation (NVT) was performed using a Berendsen thermostat of 120 ps at 300 K and tau = 1 ps^{-1}. Subsequently, a microcanonical (NPT) simulation using a Berendsen thermostat of 120 ps at 300 K and tau = 1 was performed [50]. Finally, we ran 500 ps of simulation applying a 25 $kJ \cdot mol^{-1}$ restraint to alpha carbons. The resulting structures were the starting points for the production simulations (100 ns). For restrained and nonrestrained production simulations, a Nose–Hoover thermostat was used for temperature coupling, whereas a Parrinello–Rhaman thermostat was used for pressure coupling. In all cases, long-range interactions were computed according to the particle mesh Ewald method.

NMR spectroscopy

NMR samples, data acquisition and processing

Samples for NMR experiments contained 0.3–0.8 mM ^{15}N-labelled FXN 90–195, FXN L198R or FXN 90–210 in a buffer of 100 mM NaCl, 20 mM Tris-HCl, 1.0 mM EDTA (pH 7.0), containing 5% D_2O. NMR experiments were performed at 22 °C in a Bruker 600 MHz Avance III spectrometer (Bruker Instruments, Inc., Bellerica, MA, USA) equipped with a 5-mm triple resonance cryoprobe incorporating shielded *z*-axis gradient coils. The NMR data were processed on Silicon Graphics workstations (Silicon Graphics International, Milpitas, CA, USA) using NMRPIPE [51] and analyzed using NMRVIEWJ [52,53].

Backbone amide resonance assignment

Nitrogen and amide and alpha protons chemical shift assignments of FXN 90–195 and FXN L198R were performed via three-dimensional ^{15}N-NOESY and ^{15}N-TOCSY experiments (100 and 30 ms of mixing times, respectively), based on the available chemical shifts of the full-length C-terminal domain of FXN (BMRB 4342) [54]. Also, a ^{15}N-NOESY spectrum of FXN 90–210 was recorded to assist in the assignment. Backbone ^{15}N and ^{1}H assignments for FXN 90–195 and FXN L198R have been deposited in the BMRB with accession numbers 19785 and 19786, respectively.

Determination of hydrodynamic radii

The diffusion measurements were performed using the PFG stimulated echo longitudinal encode–decode sequence [55]. Dioxane (10 μL, 2% in H_2O) was added to 300 μL of the protein sample as an internal standard [18,56]. A series of spectra were acquired with the strength of the diffusion gradient varying between 5% and 95% of its maximum value. The length of all pulses and delays in the sequence were held constant, the pulse gradient width was 4 ms and the length of the diffusion delay was calibrated for the sample to give a maximal decay of 85–90% for the protein and dioxane signals (delays of 125 and 15 ms were used, respectively). A T_2 filter was used to selectively observe the dioxane signal without interference of the protein and, thus, to reduce the experimental error, especially at high gradient strengths. Protein and dioxane spectra were acquired with 4K and 16K complex points, respectively. R_h was calculated as:

$$R_{\mathrm{h}} = (D_{\mathrm{diox}}/D_{\mathrm{prot}}) \times R_{\mathrm{h,diox}} \quad (4)$$

where D_{diox} and D_{prot} are the measured diffusion coefficients of dioxane and protein, respectively, and $R_{\mathrm{h,diox}}$ is the effective hydrodynamic radius of dioxane, taken to be 2.12 Å [56].

^{15}N spin relaxation measurements

Measurements of ^{15}N T_1, T_2 and steady-state ^{1}H-^{15}N NOE (hnNOE) of wild-type FXN 90–210, FXN L198 and FXN 90–195 were performed at a nitrogen frequency of 60.82 MHz and 22 °C, using standard pulse schemes in an interleaved manner. Both T_1 and T_2 data were acquired with six relaxation delays. For FXN 90–210 and FXN L198R, the delays used were 7, 300, 600, 900, 1200 and 1600 ms for the T_1 calculations and 15.7, 31.4, 62.8, 125.5, 156.9 and 219.7 ms for the T_2 calculations. For FXN 90–195, the delays were 7, 300, 600, 900, 1200 and 1600 ms for T_1 and 15.7, 31.4, 62.8, 78.4, 94.1 and 125.5 ms for T_2. The rate analysis routine of NMRVIEWJ was used to analyze the data [49]. The hnNOE values were determined by the ratio of peak volumes of spectra recorded with and without ^{1}H saturation, employing a net relaxation delay of 4 s for each scan in both experiments. Typically, errors were ~ 1% for T_1 and T_2 and 2–5% for hnNOE measurements.

Relaxation dispersion experiments

CPMG relaxation dispersion experiments were performed at a single static magnetic field strength of 600.13 MHz on 0.5 mM FXN 90–210, FXN L198R and FXN 90–195. A constant-time relaxation-compensated pulse program was used, setting the constant time period (T_{CPMG}) to 100 ms for wild-type FXN 90–210 and FXN L198R and 80 ms for FXN 90–195, in combination with the CPMG frequencies (ν_{CPMG}): 40, 200, 360, 520, 680, 840, 1000 and 1200 Hz for FXN 90–210;40, 80, 120, 160, 200,

240, 280, 320, 360, 400, 480, 520, 600, 680, 760, 840, 920, 1000, 1080 and 1200 Hz for FXN L198R; and 50, 200, 400, 600, 800, 1000, 1200 and 1500 Hz for FXN 90–195. Two-dimensional data sets were acquired in an interleaved manner, with a 3-s interscan delay and 256 increments in the nitrogen dimension. The observed transverse relaxation rate (R_2^{Obs}, where R_2 is the inverse of T_2) for each frequency point was obtained from the signal intensity measured at the end of the T_{CPMG} period according to:

$$R_2^{Obs}(\nu_{CPMG}) = \frac{-ln\left(\frac{I_{\nu,CPMG}}{I_0}\right)}{T_{CPMG}} \quad (5)$$

where I_0 is the signal intensity measured in a reference spectrum lacking the CPMG period and $I_{\nu,CPMG}$ is the residual intensity at the end of the CPMG pulse sequence for a specific spin-lock frequency. A two-site global fast exchange model [57] or a model in which exchange processes are absent [i.e. $R_2^{Obs}(\nu_{CPMG}) = R_2^0$, where R_2^0 is the effective transverse relaxation rate independent of the ν_{CPMG}] was fitted to the dispersion data.

The contribution of the exchange to the signal relaxation rate (R_{ex}) is estimated by:

$$R_2^{Obs}(\nu_{CPMG} \to 0) = R_{ex} + R_2^{Obs}(\nu_{CPMG} \to \infty) \quad (6)$$

where $R_2^{Obs}(\nu_{CPMG} \to \infty)$ is the intrinsic relaxation rate in the absence of exchange, at infinite ν_{CPMG}. $R_2^{Obs}(\nu_{CPMG} \to 0)$ and $R_2^{Obs}(\nu_{CPMG} \to \infty)$ were approximated to the R_2^{Obs} at the lowest and highest ν_{CPMG} values measured, respectively.

Solvent proton exchange measurements

The exchange measurements were carried out at 22 °C using the water-NOE pulse sequence [29]. The experiment was performed in an interleaved manner to obtain two spectra, with the water magnetization oriented along the $+z$ and $-z$-axes, respectively [30]. The mixing time was 60 ms. In the experiment with the water magnetization oriented parallel to the z-axis (parallel to the amide proton magnetization), the ζ_{NOE} effect of water is added to the intrinsic intensity of the cross-peaks. By contrast, in the experiment with the water oriented antiparallel to the z-axis, the ζ_{NOE} is subtracted from the intrinsic intensity of the cross-peak. Therefore, ζ_{NOE} can be calculated by taking the difference between the cross-peak intensities corresponding to both experiments normalized by the sum of the intensities. For short mixing times, ξ_{NOE} is almost exclusively a result of the chemical exchange.

Nitrogen relaxation rates and hydrodynamic radii predictions

HYDRONMR software [25,26] was used to predict the ^{15}N T_1/T_2 ratios and HYDROPRO [19] to calculate the hydrodynamic radius of FXN 90–210. In both cases, the coordinates from the crystallographic structure (PDB code: 1EGK) were used in the calculations; the temperature was set at 23 °C, viscosity at 9.66×10^{-4} kg·m^{-1}·s^{-1} and the atomic element radius was 3.2 Å.

Iron-binding capability assay for FXN variants

To determine the stability of iron-FXN complexes in solution, protein (50 μM) in buffer 50 mM Hepes, 50 mM NaCl (pH 7.0) was incubated with $FeCl_3$ (250 μM) to a final volume of 150 μL in individual microcentrifuge tubes of 500 μL. After incubation (0–120 min) at 25 °C, samples were centrifuged for 5 min at 20 000 ***g*** and 25 °C, and soluble iron was quantified. In addition, protein concentration was analyzed by SDS/PAGE to evaluate protein aggregation and precipitation during the incubation with the metal ion.

To estimate the stoichiometry in which FXN variants maintain Fe^{+3} soluble and bioavailable, increasing protein concentrations (between 0 and 100 μM) of each FXN variant were incubated with $FeCl_3$ (250 μM) in buffer 50 mM Hepes, 50 mM NaCl (pH 7.0) at 25 °C in individual tubes of 500 μM for 30 min at 25 °C. Afterwards, samples were centrifuged at 20 000 ***g*** and 25 °C for 5 min and soluble iron was quantified.

Because BSA possesses iron-binding capability, this protein was used as a positive control, whereas hen egg-white lysozyme was included in the experiment as a negative control.

Determination of iron

Iron concentration was determined using a colorimetric method based on the coordination of Fe^{2+} by 1,10-phenanthroline. Briefly, 1,10-phenanthroline was prepared in 0.1 M HCl and a standard iron solution (18 mM) was prepared in 10 mM sulfuric acid for calibration curves. For iron quantification, 100-μL samples were used, in a final volume of 1 mL. Following vortexing and 30 min of incubation at room temperature, the sample was centrifuged at 20 000 ***g*** for 10 min. This centrifugation step is important because

protein aggregates may disperse light, generate scattering in the sample and thus lead to incorrect iron determinations. Next, A_{512} was monitored. Blanks were routinely included in the measurements.

Acknowledgements

This work was supported by the Agencia Nacional de Promoción Científica y Tecnológica (ANPCyT), the Consejo Nacional de Investigaciones Científicas y Técnicas (CONICET) and the Universidad de Buenos Aires (UBACyT). We especially thank Dr Hélène Puccio for kindly providing us with the FXN gene.

Author contributions

SEF performed experiments and analyzed data. EAR performed experiments and analyzed data. MA performed experiments and analyzed data. MG planed experiments, analyzed data and wrote the paper. JS planed experiments, analyzed data and wrote the paper.

References

1 Condo I, Ventura N, Malisan F, Rufini A, Tomassini B & Testi R (2007) In vivo maturation of human frataxin. *Hum Mol Genet* **16**, 1534–1540.
2 Schmucker S, Argentini M, Carelle-Calmels N, Martelli A & Puccio H (2008) The in vivo mitochondrial two-step maturation of human frataxin. *Hum Mol Genet* **17**, 3521–3531.
3 Bencze KZ, Fau-Yoon T, Yoon T, Fau-Millan-Pacheco C, Millan-Pacheco C, Fau-Bradley PB, Bradley PB, Fau-Pastor N, Pastor N, Fau-Cowan JA *et al.* (2007) Human frataxin: iron and ferrochelatase binding surface. *Chem Commun (Camb)* **14**, 1798–1800.
4 Gakh O, Bedekovics T, Duncan SF, Smith DY, Berkholz DS & Isaya G (2010) Normal and Friedreich ataxia cells express different isoforms of frataxin with complementary roles in iron-sulfur cluster assembly. *J Biol Chem* **285**, 38486–38501.
5 Yoon T & Cowan JA (2003) Iron-sulfur cluster biosynthesis. Characterization of frataxin as an iron donor for assembly of [2Fe-2S] clusters in ISU-type proteins. *J Am Chem Soc* **125**, 6078–6084.
6 Musco G, Stier G, Kolmerer B, Adinolfi S, Martin S, Frenkiel T, Gibson T & Pastore A (2000) Towards a structural understanding of Friedreich's ataxia: the solution structure of frataxin. *Structure* **8**, 695–707.
7 Bridwell-Rabb J, Winn AM & Barondeau DP (2011) Structure-function analysis of Friedreich's ataxia mutants reveals determinants of frataxin binding and activation of the Fe-S assembly complex. *Biochemistry* **50**, 7265–7274.
8 Dhe-Paganon S, Shigeta R, Chi YI, Ristow M & Shoelson SE (2000) Crystal structure of human frataxin. *J Biol Chem* **275**, 30753–30756.
9 Tsai CL, Bridwell-Rabb J & Barondeau DP (2011) Friedreich's ataxia variants I154F and W155R diminish frataxin-based activation of the iron-sulfur cluster assembly complex. *Biochemistry* **50**, 6478–6487.
10 Pandolfo M & Pastore A (2009) The pathogenesis of Friedreich ataxia and the structure and function of frataxin. *J Neurol* **256** (Suppl 1), 9–17.
11 Adinolfi S, Nair M, Politou A, Bayer E, Martin S, Temussi P & Pastore A (2004) The factors governing the thermal stability of frataxin orthologues: how to increase a protein's stability. *Biochemistry* **43**, 6511–6518.
12 Roman EA, Faraj SE, Gallo M, Salvay AG, Ferreiro DU & Santos J (2012) Protein stability and dynamics modulation: the case of human frataxin. *PLoS ONE* **7**, e45743.
13 Correia AR, Adinolfi S, Pastore A & Gomes CM (2006) Conformational stability of human frataxin and effect of Friedreich's ataxia-related mutations on protein folding. *Biochem J* **398**, 605–611.
14 Correia AR, Pastore C, Adinolfi S, Pastore A & Gomes CM (2008) Dynamics, stability and iron-binding activity of frataxin clinical mutants. *FEBS J* **275**, 3680–3690.
15 Al-Mahdawi S, Pook M & Chamberlain S (2000) A novel missense mutation (L198R) in the Friedreich's ataxia gene. *Hum Mutat* **16**, 95.
16 Sacca F, Marsili A, Puorro G, Antenora A, Pane C, Tessa A, Scoppettuolo P, Nesti C, Brescia Morra V, De Michele G *et al.* (2013) Clinical use of frataxin measurement in a patient with a novel deletion in the FXN gene. *J Neurol* **260**, 1116–1121.
17 Kamerzell TJ & Middaugh CR (2008) The complex inter-relationships between protein flexibility and stability. *J Pharm Sci* **97**, 3494–3517.
18 Wilkins DK, Grimshaw SB, Receveur V, Dobson CM, Jones JA & Smith LJ (1999) Hydrodynamic radii of native and denatured proteins measured by pulse field gradient NMR techniques. *Biochemistry* **38**, 16424–16431.
19 Ortega A, Amoros D & Garcia de la Torre J (2011) Prediction of hydrodynamic and other solution properties of rigid proteins from atomic- and residue-level models. *Biophys J* **101**, 892–898.
20 Shen Y, Delaglio F, Cornilescu G & Bax A (2009) TALOS+: a hybrid method for predicting protein backbone torsion angles from NMR chemical shifts. *J Biomol NMR* **44**, 213–223.

21 Santos J, Risso VA, Sica MP & Ermacora MR (2007) Effects of serine-to-cysteine mutations on beta-lactamase folding. *Biophys J* **93**, 1707–1718.
22 You C, Huang Q, Xue H, Xu Y & Lu H (2010) Potential hydrophobic interaction between two cysteines in interior hydrophobic region improves thermostability of a family 11 xylanase from Neocallimastix patriciarum. *Biotechnol Bioeng* **105**, 861–870.
23 Myers JK, Pace CN & Scholtz JM (1995) Denaturant m values and heat capacity changes: relation to changes in accessible surface areas of protein unfolding. *Protein Sci* **4**, 2138–2148.
24 Schymkowitz J, Borg J, Stricher F, Nys R, Rousseau F & Serrano L (2005) The FoldX web server: an online force field. *Nucleic Acids Res* **33**, W382–W388.
25 Garcia de la Torre J, Huertas ML & Carrasco B (2000) HYDRONMR: prediction of NMR relaxation of globular proteins from atomic-level structures and hydrodynamic calculations. *J Magn Reson* **147**, 138–146.
26 Garcia De La Torre J, Huertas ML & Carrasco B (2000) Calculation of hydrodynamic properties of globular proteins from their atomic-level structure. *Biophys J* **78**, 719–730.
27 Viles JH, Donne D, Kroon G, Prusiner SB, Cohen FE, Dyson HJ & Wright PE (2001) Local structural plasticity of the prion protein. Analysis of NMR relaxation dynamics. *Biochemistry* **40**, 2743–2753.
28 Palmer AG 3rd, Kroenke CD & Loria JP (2001) Nuclear magnetic resonance methods for quantifying microsecond-to-millisecond motions in biological macromolecules. *Methods Enzymol* **339**, 204–238.
29 Grzesiek S & Bax A (1993) Measurement of amide proton exchange rates and NOEs with water in 13C/15N-enriched calcineurin B. *J Biomol NMR* **3**, 627–638.
30 Gallo M, Pennestri M, Bottomley MJ, Barbato G, Eliseo T, Paci M, Narjes F, De Francesco R, Summa V, Koch U *et al.* (2009) Binding of a noncovalent inhibitor exploiting the S' region stabilizes the hepatitis C virus NS3 protease conformation in the absence of cofactor. *J Mol Biol* **385**, 1142–1155.
31 Baldwin AJ & Kay LE (2009) NMR spectroscopy brings invisible protein states into focus. *Nat Chem Biol* **5**, 808–814.
32 Mittermaier AK & Kay LE (2009) Observing biological dynamics at atomic resolution using NMR. *Trends Biochem Sci* **34**, 601–611.
33 Rufini A, Fortuni S, Arcuri G, Condo I, Serio D, Incani O, Malisan F, Ventura N & Testi R (2011) Preventing the ubiquitin-proteasome-dependent degradation of frataxin, the protein defective in Friedreich's ataxia. *Hum Mol Genet* **20**, 1253–1261.
34 Dagan S, Hagai T, Gavrilov Y, Kapon R, Levy Y & Reich Z (2013) Stabilization of a protein conferred by an increase in folded state entropy. *Proc Natl Acad Sci USA* **110**, 10628–10633.
35 Durney MA, Wechselberger RW, Kalodimos CG, Kaptein R, Vorgias CE & Boelens R (2004) An alternate conformation of the hyperthermostable HU protein from Thermotoga maritima has unexpectedly high flexibility. *FEBS Lett* **563**, 49–54.
36 Hernandez G, Jenney FE Jr, Adams MW & LeMaster DM (2000) Millisecond time scale conformational flexibility in a hyperthermophile protein at ambient temperature. *Proc Natl Acad Sci USA* **97**, 3166–3170.
37 Whitley MJ, Zhang J & Lee AL (2008) Hydrophobic core mutations in CI2 globally perturb fast side-chain dynamics similarly without regard to position. *Biochemistry* **47**, 8566–8576.
38 Prischi F, Giannini C, Adinolfi S & Pastore A (2009) The N-terminus of mature human frataxin is intrinsically unfolded. *FEBS J* **276**, 6669–6676.
39 Anandakrishnan R, Aguilar B & Onufriev AV (2012) H++ 3.0: automating pK prediction and the preparation of biomolecular structures for atomistic molecular modeling and simulations. *Nucleic Acids Res* **40**, W537–W541.
40 Davies MN, Toseland CP, Moss DS & Flower DR (2006) Benchmarking pK(a) prediction. *BMC Biochem* **7**, 18.
41 Li H, Robertson AD & Jensen JH (2005) Very fast empirical prediction and rationalization of protein pKa values. *Proteins* **61**, 704–721.
42 Prischi F, Konarev PV, Iannuzzi C, Pastore C, Adinolfi S, Martin SR, Svergun DI & Pastore A (2010) Structural bases for the interaction of frataxin with the central components of iron-sulphur cluster assembly. *Nat Commun* **95**, 1–10.
43 Colin F, Martelli A, Clémancey M, Latour JM, Gambarelli S, Zeppieri L, Birck C, Page A, Puccio H & Ollagnier de Choudens S (2013) Mammalian frataxin controls sulfur production and iron entry during de novo Fe4S4 cluster assembly. *J Am Chem Soc* **135**, 733–740.
44 Schmucker S, Martelli A, Colin F, Page A, Wattenhofer-Donzé M, Reutenauer L & Puccio H (2011) Mammalian frataxin: an essential function for cellular viability through an interaction with a preformed ISCU/NFS1/ISD11 iron-sulfur assembly complex. *PLoS ONE* **6**, e16199.
45 Eftink MR & Ghiron CA (1981) Fluorescence quenching studies with proteins. *Anal Biochem* **114**, 199–227.
46 Santoro MM & Bolen DW (1992) A test of the linear extrapolation of unfolding free energy changes over an extended denaturant concentration range. *Biochemistry* **31**, 4901–4907.
47 Fersht A (1999) Structure and Mechanism in Protein Science: A Guide to Enzyme Catalysis and Protein Folding. WH Freeman, New York.

48 Van Der Spoel D, Lindahl E, Hess B, Groenhof G, Mark AE & Berendsen HJ (2005) GROMACS: fast, flexible, and free. *J Comput Chem* **26**, 1701–1718.
49 Oostenbrink C, Villa A, Mark AE & van Gunsteren WF (2004) A biomolecular force field based on the free enthalpy of hydration and solvation: the GROMOS force-field parameter sets 53A5 and 53A6. *J Comput Chem* **25**, 1656–1676.
50 Berendsen HJC, Postma JPM, Gunsteren WFV, DiNola A & Haak JR (1984) Molecular dynamics with coupling to an external bath. *J Chem Phy* **81**, 3684–3690.
51 Delaglio F, Grzesiek S, Vuister GW, Zhu G, Pfeifer J & Bax A (1995) NMRPipe: a multidimensional spectral processing system based on UNIX pipes. *J Biomol NMR* **6**, 277–293.
52 Johnson BA (2004) Using NMRView to visualize and analyze the NMR spectra of macromolecules. *Methods Mol Biol* **278**, 313–352.
53 Kirby NI, DeRose EF, London RE & Mueller GA (2004) NvAssign: protein NMR spectral assignment with NMRView. *Bioinformatics* **20**, 1201–1203.
54 Musco G, de Tommasi T, Stier G, Kolmerer B, Bottomley M, Adinolfi S, Muskett FW, Gibson TJ, Frenkiel TA & Pastore A (1999) Assignment of the 1H, 15N, and 13C resonances of the C-terminal domain of frataxin, the protein responsible for Friedreich ataxia. *J Biomol NMR* **15**, 87–88.
55 Merrill MR (1993) NMR Diffusion Measurements Using a Composite Gradient PGSE Sequence. *J Magn Reson, Ser A* **103**, 223–225.
56 Jones J, Wilkins D, Smith L & Dobson C (1997) Characterisation of protein unfolding by NMR diffusion measurements. *J Biomol NMR* **10**, 199–203.
57 Luz Z & Meiboom S (1963) Nuclear magnetic resonance study of the protolysis of trimethylammonium ion in aqueous solution – order of the reaction with respect to solvent. *J Chem Phys* **39**, 366–370.
58 Uversky VN (1993) Use of fast protein size-exclusion liquid chromatography to study the unfolding of proteins which denature through the molten globule. *Biochemistry* **32**, 13288–13298.